Location Awareness in Beyond 5G Networks via Reconfigurable Intelligent Surfaces

Ziyi Wang, *Graduate Student Member, IEEE*, Zhenyu Liu, *Graduate Student Member, IEEE*, Yuan Shen, *Senior Member, IEEE*, Andrea Conti, *Fellow, IEEE*, and Moe Z. Win, *Fellow, IEEE*

***Abstract*— Achieving accurate location-awareness in wireless networks requires integrated sensing and communication (ISAC), where optimization, signal processing, and data fusion are performed under a common framework. The efficiency of ISAC in complex wireless environments can be improved via the use of reconfigurable intelligent surfaces (RISs). This paper introduces the concept of continuous intelligent surface (CIS) and establishes the fundamental limits of RIS-aided ISAC systems, specifically, an RIS-aided localization and communication system. In particular, this paper considers two types of RISs, namely CISs and discrete intelligent surfaces (DISs). First, this paper proposes a general signal model for RIS-aided localization and communication valid for both near-field and far-field scenarios, and then theoretical limits on the localization and communication performance are derived. Based on the proposed model, Fisher information analyses of the localization performance in networks with RISs are performed. Numerical results show that RISs with optimized phase responses can improve the received signal-to-noise ratio (SNR) and spectral efficiency of communication, and the localization accuracy significantly.**

***Index Terms*— Beyond 5G, integrated sensing and communication, network localization, reconfigurable intelligent surface, Fisher information.**

I. Introduction

SENSING AND COMMUNICATION are required in a variety of applications such as location-based services [1]–[4], object detection and tracking [5]–[10], smart environments [11]–[14], and Internet-of-Things (IoT) [15]–[19]. However, in complex wireless environments, the sensing and communication systems may not achieve the required performance [20]. For example, for indoor location sensing, global navigation satellite systems (GNSSs) [21]–[23] can fail to provide sufficient position information due to the weak signals from the satellites. Existing works focus mainly on the design of sensing and communication techniques that are resilient and robust to harsh electromagnetic (EM) environments caused by multipath effect, cluttering, and non-line-of-sight propagation. However, the optimization and design of conventional indoor sensing and communication systems are still constrained by complicated and unfavorable EM environments. intelligent surfaces (ISs) enable a fully-controllable EM environment and are considered a potential candidate for beyond 5G wireless communications.

Localization is an important application that can benefit from the improved sensing and communication capabilities due to the employment of ISs. The design and analysis of accurate localization has been investigated extensively in recent decades [24]–[37]. A promising paradigm for obtaining reliable position information even in harsh wireless environments is network localization and navigation (NLN). In particular, NLN advocates spatiotemporal cooperation among users, fusion of multimodal sensor measurements via soft information, and efficient management of resources via network operation techniques [38]–[40]. It is envisioned that ISs can be integrated into the paradigm of NLN to further improve the localization performance.

In general, ISs can be categorized as active ISs and nearly-passive ISs. Active ISs, also known as large intelligent surfaces (LISs), can radiate and receive EM waves based on low-power circuit techniques [41], and they can be viewed as massive multiple-input mulitple-output with denser antennas. The use of LISs is considered for both localization [42] and communication [43], where the LISs are modeled as continuous surfaces. In previous works, the controllable phase responses of LISs [44], [45] were not exploited to affect the state of channels and thus the potential of ISs for improving the EM environment was not fully unleashed. Nearly-passive ISs, also known as reconfigurable intelligent surfaces (RISs), arise in recent years as an important candidate for beyond 5G communications. In particular, they can be used to improve the accuracy of localization systems due to their reconfigurability, low power consumption, and inexpensive fabrication [46]. Compared to LISs, RISs can be used to control the phase

Manuscript received August 22, 2021; revised December 10, 2021; accepted January 14, 2022. Date of publication March 8, 2022; date of current version June 17, 2022. This work was supported in part by the Office of Naval Research under Grant N00014-16-1-2141 and Grant N62909-22-1-2009, in part by the European Union's Horizon 2020 Research and Innovation Program under Grant 871249, and in part by the National Natural Science Foundation of China under Grant 61871256. An earlier version of this paper was presented in part at the IEEE International Conference on Communications, Seoul, South Korea, May 2022. *(Corresponding author: Moe Z. Win.)*

Ziyi Wang and Zhenyu Liu are with the Wireless Information and Network Sciences Laboratory, Massachusetts Institute of Technology, Cambridge, MA 02139 USA (e-mail: ziyiwang@mit.edu; zliu14@mit.edu).

Yuan Shen is with the Department of Electronic Engineering, Tsinghua University, Beijing 100084, China (e-mail: shenyuan_ee@tsinghua.edu.cn).

Andrea Conti is with the Department of Engineering and CNIT, University of Ferrara, 44122 Ferrara, Italy (e-mail: a.conti@ieee.org).

Moe Z. Win is with the Laboratory for Information and Decision Systems (LIDS), Massachusetts Institute of Technology, Cambridge, MA 02139 USA (e-mail: moewin@mit.edu).

Color versions of one or more figures in this article are available at https://doi.org/10.1109/JSAC.2022.3155542.

Digital Object Identifier 10.1109/JSAC.2022.3155542

0733-8716 © 2022 IEEE. Personal use is permitted, but republication/redistribution requires IEEE permission.
See https://www.ieee.org/publications/rights/index.html for more information.

Authorized licensed use limited to: MIT Libraries. Downloaded on June 19,2022 at 19:18:15 UTC from IEEE Xplore. Restrictions apply.

and amplitude of incident EM waves with lower overhead. RISs have been viewed as discrete arrays in most recent work [47]–[50]. In particular, some problems of sensing [47] and communications [48], [49] aided by RISs have been studied using the far-field model, while further considerations and new research directions are given in [51]. A near-field model has been adopted for studying RIS-aided localization in [50]. In [47]–[50], the polarization of the received antenna is not accounted for, the spatial variation of pathloss and phase on RIS is not fully considered, and analysis based on the EM theory is missing.

The fundamental questions related to integrated sensing and communication (ISAC) with RISs are as follows: (i) what is the general signal model at the receiver in the presence of RISs; and (ii) how do RISs improve the localization and communication capabilities of the systems? The answers to these questions provide insights into the design and analysis of RIS-aided ISAC. The goal of this paper is to determine the fundamental limits of RIS-aided localization and performance improvement of RIS-aided communication. We advocate RIS-aided NLN, a new paradigm in which the EM environment is controlled via RISs for localization and communication. The key idea is to carefully control the phase response of an RIS so that signals, scattered by different parts of the surface, superimpose coherently at the receivers.

This paper introduces the concept of continuous intelligent surfaces (CISs) and establishes the performance limits of RIS-aided communication and RIS-aided localization in beyond 5G networks.[1] The key contributions of the paper include:

- a near/far-field signal model and the theoretical limits for localization and communications via two types of RISs, namely CISs and discrete intelligent surfaces (DISs);
- optimal design of the phase response for RISs in different scenarios including those with obstacles and multiple surfaces; and
- quantification of performance gain of localization and communication offered by RISs in complex wireless environments.

The remainder of this paper is organized as follows. Section II introduces the concept of CIS and presents the general signal model for RIS-aided localization and communication. Section III presents the signal-to-noise ratio (SNR) and spectral efficiency of CIS-aided communication, performs Fisher information analysis of CIS-aided localization systems, and investigates a case study of localization with a CIS. Section IV discusses two extensive scenarios considering obstacles as well as interaction among CISs and scattering planes. Numerical results are provided in Section V. Section VI gives some final remarks.

Notations: Throughout this paper, variables, random variables, random vectors, matrices, vectors and their unit vectors are written as italic letters x, sans-serif upright letters x, bold sans-serif upright letters $\boldsymbol{\mathsf{x}}$, bold capital italic letters $\boldsymbol{X}$, bold italic letters $\boldsymbol{x}$ and $\tilde{\boldsymbol{x}}$, respectively. Let $\boldsymbol{A}^*$, $\boldsymbol{A}^{\mathrm{T}}$ and $\boldsymbol{A}^{\mathrm{H}}$, denote the conjugate, transpose, and conjugate transpose of matrix $\boldsymbol{A}$, respectively. Notation $\boldsymbol{A} \succcurlyeq \boldsymbol{B}$ denotes that $\boldsymbol{A} - \boldsymbol{B}$ is positive semi-definite. Notation $\boldsymbol{0}_m$ denotes a vector of length m with all 0's; $|\boldsymbol{x}|$ denotes the Euclidean norm of $\boldsymbol{x}$; $\jmath$ denotes imaginary unit. The operators ∇, $\nabla\times$, $\nabla\cdot$, and $\otimes$ denote the gradient, curl, divergence, and cross product, respectively. In addition, $\Re\{x\}$ and $\arg\{x\}$ represent the real part and argument of a complex number x, respectively. The expectation of a random vector $\boldsymbol{\mathsf{x}}$ is denoted by $\mathbb{E}\{\boldsymbol{\mathsf{x}}\}$. The notations of important quantities are summarized in Table I.

[1]Our approach considers CISs where the controlled phase response function is continuous over the entire surface, rather than approximating metasurfaces composed of discrete elements with a continuous model via homogenization as in [46].

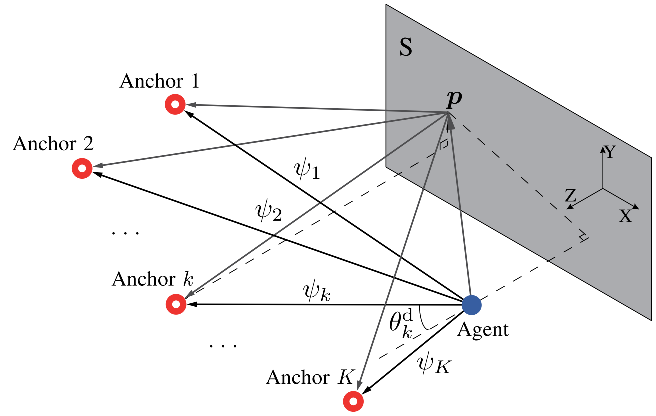

Fig. 1. The localization and communication system with a CIS. In contrast to a scattering plane, the phase shift of EM field over the entire surface can be controlled with a CIS. The agent can be placed in the near field (spherical wave-fronts) or the far field (planar wave-fronts) of the CIS.

II. System Model

This section first proposes the general signal model for the ISAC system with an RIS based on the EM theory, and then reveals the relationship between the signal models of ISAC systems with CISs and DISs. A CIS refers to an RIS whose phase response is a continuous two-dimensional function of each point of the surface. A DIS refers to an RIS whose phase response function is piece-wise constant. In practical systems, DISs whose elements are densely arranged on the surfaces, such as those with the spacing of elements set to half of the operating wavelength, can be viewed as an approximation of CISs. CISs can serve as benchmarks when evaluating the effects of element size on the localization and communication performance.

A. General Signal Model of Localization and Communication With a CIS

Consider a three-dimensional (3D) scenario with one CIS, one agent that acts as a transmitter and K anchors that act as receivers, as shown in Fig. 1. The agent is a node with an unknown position, and the anchors are nodes with known positions. Denote the coordinates of a point on the CIS, the agent, and the k-th anchor by $\boldsymbol{p}, \boldsymbol{q}, \boldsymbol{p}_k \in \mathbb{R}^3$, respectively. Without loss of generality, set the CIS in the X-Y plane of the coordinate system, as shown in Fig. 1, so that $\boldsymbol{p}$ can be written as $[\breve{\boldsymbol{p}}^{\mathrm{T}}, 0]^{\mathrm{T}}$, where $\breve{\boldsymbol{p}}$ denotes the x- and y-coordinates of $\boldsymbol{p}$. In addition, $\boldsymbol{q}$ and $\boldsymbol{p}_k$ can be expressed as $\boldsymbol{q} = [q_1, q_2, q_3]^{\mathrm{T}}$ and $\boldsymbol{p}_k = [x_k, y_k, z_k]^{\mathrm{T}}$, respectively. The objective of the ISAC system is to communicate between the agent and anchors and to localize the agent using the received signals of the anchors.

Authorized licensed use limited to: MIT Libraries. Downloaded on June 19,2022 at 19:18:15 UTC from IEEE Xplore. Restrictions apply.

TABLE I
NOTATIONS OF IMPORTANT QUANTITIES

Notation	Definition	Notation	Definition
f_c	Carrier frequency of the transmitted signal	N_0	One-sided PSD of complex white Gaussian noise
$\boldsymbol{q}$	Position of the agent	$\boldsymbol{p}$	3D coordinate of a point on the CIS
$\boldsymbol{p}_k$	Position of the k-th anchor	$\rho_{\mathrm{T}}(\boldsymbol{p})$	Distance of a point on the CIS and the agent
$\rho_{\mathrm{R},k}(\boldsymbol{p})$	Distance of a point on the CIS and the k-th anchor	$\rho_{\mathrm{D},k}$	Distance of the agent and the k-th anchor
$r_k^{\mathrm{s}}(t)$	Signal received at the k-th anchor from the scattering path	$r_k^{\mathrm{d}}(t)$	Signal received at the k-th anchor from the direct path
ψ_k	Channel index of the direct path between k-th anchor and the agent	P_{T}	Transmitting power of the antenna of the agent
$\gamma_k^{\mathrm{s}}(\boldsymbol{p})$	Loss due to the polarization difference of the antenna at the k-th anchor and the transmitted EM waves via the scattering path	γ_k^{d}	Loss due to the polarization difference of the antenna at the k-th anchor and the transmitted EM waves via the direct path
$F_k^{\mathrm{s}}(\boldsymbol{p})$	Directive gain of the antennas of the k-th anchor and the agent on the scattering path	F_k^{d}	Directive gain of the antennas of the k-th anchor and the agent on the direct path
$\mathcal{S}$	Set of two-dimensional coordinates of all points on the CIS	$\Phi_{\mathrm{R}}(\breve{\boldsymbol{p}})$	Phase response function of the CIS, where $\breve{\boldsymbol{p}} \in \mathcal{S}$
$\boldsymbol{J}_k(\boldsymbol{q})$	FIM on localization error at the k-th anchor	$\boldsymbol{C}_k(\boldsymbol{q})$	Information matrix from the coupling of the direct path and the scattering path between the agent and the k-th anchor
$\boldsymbol{J}_k^{\mathrm{O}}(\boldsymbol{q})$	FIM on localization error with OSPs at the k-th anchor	$\boldsymbol{J}_k^{\mathrm{M}}(\boldsymbol{q})$	FIM on localization error with multiple CISs at the k-th anchor
$\boldsymbol{J}_k^{\mathrm{s}}(\boldsymbol{q})$	FIM on localization error at the k-th anchor from the scattering path	$\boldsymbol{J}_k^{\mathrm{d}}(\boldsymbol{q})$	FIM on localization error at the k-th anchor from the direct path

Consider a narrow-band system where the phase of scattered EM field on the CIS can be controlled and the paths between the CISs and the agents are in free-space propagation. If the paths between the agent and the anchors are obstructed, the signals on the paths are eliminated. Otherwise, the paths from the agent to all anchors allow free-space propagation. In addition, consider the following. (A1) The size of the CIS D is much larger than the signal center wavelength λ_0, i.e., $D \gg \lambda_0$. (A2) The anchor is deployed in the far field of the CIS, so the distance between the k-th anchor and a point $\boldsymbol{p}$ on the CIS $\rho_{\mathrm{R},k}(\boldsymbol{p})$ is much larger than the signal wavelength, i.e., $\rho_{\mathrm{R},k}(\boldsymbol{p}) \gg \lambda_0$.

Lemma 1: Consider a CIS illuminated by a finite antenna. For any position of the source in radiating near/far-field region, the far-field scattered EM waves of the CIS are given by

$$\boldsymbol{h}^{\mathrm{s}} = \frac{-\jmath\beta}{2\pi}\int_{\mathcal{S}}\left[\tilde{\boldsymbol{r}} \otimes (\tilde{\boldsymbol{n}} \otimes \boldsymbol{h}^{\mathrm{i}})\right]\frac{e^{-\jmath\beta|\boldsymbol{r}-\boldsymbol{p}|}}{|\boldsymbol{r}-\boldsymbol{p}|}e^{\jmath\Phi_{\mathrm{R}}(\breve{\boldsymbol{p}})}\,d\breve{\boldsymbol{p}} \tag{1}$$

$$\boldsymbol{e}^{\mathrm{s}} = \frac{\jmath\beta\eta}{2\pi}\int_{\mathcal{S}}\left[\tilde{\boldsymbol{r}}\otimes\left[\tilde{\boldsymbol{r}}\otimes(\tilde{\boldsymbol{n}}\otimes\boldsymbol{h}^{\mathrm{i}})\right]\right]\frac{e^{-\jmath\beta|\boldsymbol{r}-\boldsymbol{p}|}}{|\boldsymbol{r}-\boldsymbol{p}|}e^{\jmath\Phi_{\mathrm{R}}(\breve{\boldsymbol{p}})}\,d\breve{\boldsymbol{p}} \tag{2}$$

where $\breve{\boldsymbol{p}} \in \mathcal{S}$ and $\mathcal{S}$ is the set of two-dimensional coordinates of all points on the CIS; $\Phi_{\mathrm{R}}(\breve{\boldsymbol{p}})$ is the reflective phase response function of the CIS, $\Phi_{\mathrm{R}}(\breve{\boldsymbol{p}}) : \mathcal{S} \to [0, 2\pi)$, and the function $\Phi_{\mathrm{R}}(\breve{\boldsymbol{p}})$ can be dynamically controlled; $\boldsymbol{h}^{\mathrm{i}}$ is the incident magnetic wave; $\boldsymbol{r}$, $\tilde{\boldsymbol{n}}$, β, and η are the field point, the surface normal, the wave number, and the wave impedance, respectively. In addition, the term $\exp\{\jmath 2\pi f_c t\}$ which should be multiplied in (1) and (2) is omitted for brevity.

Proof: See Appendix A.

Remark 1: Lemma 1 describes the relation of the input and output EM waves for a CIS. In particular, the phase response function of the CIS is embodied in the scattered EM waves. It is noteworthy that when the phase response function $\Phi_{\mathrm{R}}(\breve{\boldsymbol{p}}) = 0$, $\breve{\boldsymbol{p}} \in \mathcal{S}$, Lemma 1 describes a scattering plane.

With (A1)-(A2), Lemma 1 could be used to describe the scattering field of an illuminated CIS at the k-th anchor. Therefore, the received signal at the k-th anchor is

$$\mathsf{r}_k(t) = r_k^{\mathrm{s}}(t) + \psi_k r_k^{\mathrm{d}}(t) + \mathsf{n}_k(t) \tag{3}$$

with

$$\psi_k = \begin{cases} 1, & \text{LOS} \\ 0, & \text{otherwise} \end{cases} \tag{4}$$

for any t within an observation interval $[0, T_{\mathrm{obs}})$. Here $r_k^{\mathrm{s}}(t)$ is the signal component scattered by the agent-illuminated CIS, $r_k^{\mathrm{d}}(t)$ is the signal component radiated from the agent, and $\mathsf{n}_k(t)$ is modeled as complex white Gaussian noise with one-sided power spectral density (PSD) N_0. Eq. (4) indicates that if the agent and anchor are not in line-of-sight (LOS), there is no signal transmitted from the agent to the k-th anchor by the direct path. The next proposition presents the expressions of $r_k^{\mathrm{s}}(t)$ and $r_k^{\mathrm{d}}(t)$.

Proposition 1: The signal component $r_k^{\mathrm{s}}(t)$ scattered by the agent-illuminated CIS and the signal component $r_k^{\mathrm{d}}(t)$ radiated directly from the agent can be written respectively as

$$r_k^{\mathrm{s}}(t) = \frac{\jmath k_0\sqrt{P_{\mathrm{T}}}}{4\pi\sqrt{2R_{\mathrm{L}}}}\int_{\mathcal{S}}\gamma_k^{\mathrm{s}}(\boldsymbol{p})F_k^{\mathrm{s}}(\boldsymbol{p}) \times\frac{e^{-\jmath k_0(\rho_{\mathrm{T}}(\boldsymbol{p})+\rho_{\mathrm{R},k}(\boldsymbol{p}))}}{\rho_{\mathrm{T}}(\boldsymbol{p})\rho_{\mathrm{R},k}(\boldsymbol{p})}e^{\jmath\Phi_{\mathrm{R}}(\breve{\boldsymbol{p}})}\,d\breve{\boldsymbol{p}} \tag{5}$$

$$r_k^{\mathrm{d}}(t) = \frac{\sqrt{P_{\mathrm{T}}}}{2\sqrt{2R_{\mathrm{L}}}}\gamma_k^{\mathrm{d}}F_k^{\mathrm{d}}\frac{e^{-\jmath k_0\rho_{\mathrm{D},k}}}{\rho_{\mathrm{D},k}} \tag{6}$$

where P_{T} is the transmitting power of the antenna of the agent; R_{L} is the load resistance of the receiver (Rx) antenna; $\gamma_k^{\mathrm{s}}(\boldsymbol{p})$ and γ_k^{d} are the losses due to the polarization difference of the antenna at the k-th anchor and the transmitted EM waves via the scattering path and the direct path, respectively; $F_k^{\mathrm{s}}(\boldsymbol{p})$ and F_k^{d} are directive gains of the antennas of the anchors and of the agent on the scattering path and direct path, respectively; $\rho_{\mathrm{T}}(\boldsymbol{p})$ is the distance between the agent and a point $\boldsymbol{p}$ on the CIS; $\rho_{\mathrm{D},k}$ is the distance between the agent and the k-th anchor; $k_0 = 2\pi/\lambda_0 = 2\pi f_{\mathrm{c}}/c_0$, and k_0, f_{c} and c_0 are vacuum wave number, carrier frequency, and vacuum speed of light, respectively.

Proof: See Appendix B.

Remark 2: The signal model of $r_k^{\mathrm{s}}(t)$ scattered by the agent-illuminated CIS is also a general model for RISs. RISs whose

Authorized licensed use limited to: MIT Libraries. Downloaded on June 19,2022 at 19:18:15 UTC from IEEE Xplore. Restrictions apply.

elements are densely arranged, i.e., DISs, can be described by the proposed model with a special phase response function whose value is constant in each element. Besides, the proposed model is more precise than the signal models for DISs which consider the surfaces as discrete arrays, because it describes the difference of pathloss and phase within the area of an element on a DIS.

B. Signal Model of Localization and Communication With a DIS

In practice, a CIS is implemented by plenty of subwavelength-size discrete elements, so it can also be considered as an $N_\mathrm{a} \times N_\mathrm{b}$ discrete reflecting array under the same assumption. Specially, for far-field scenarios, the signal model with a CIS is usually expressed as a discrete form, which can be viewed as an approximation from the continuous model. We partition a rectangular CIS into an array consisting of $N_\mathrm{a} \times N_\mathrm{b}$ elements. Let $\mathcal{S}_{ij}$ represent the set of all points on the element at the i-th row and the j-th column of the CIS. Then

$$r_k^\mathrm{s}(t) = \frac{\jmath k_0 \sqrt{P_\mathrm{T}}}{4\pi\sqrt{2R_\mathrm{L}}} \sum_{i=1}^{N_\mathrm{a}} \sum_{j=1}^{N_\mathrm{b}} \int_{\mathcal{S}_{ij}} \frac{\gamma_k^\mathrm{s}(\boldsymbol{p}) F_k^\mathrm{s}(\boldsymbol{p})}{\rho_\mathrm{T}(\boldsymbol{p})\rho_{\mathrm{R},k}(\boldsymbol{p})} \times e^{-\jmath k_0(\rho_\mathrm{T}(\boldsymbol{p})+\rho_{\mathrm{R},k}(\boldsymbol{p}))+\jmath\Phi_\mathrm{R}(\breve{\boldsymbol{p}})}\, d\breve{\boldsymbol{p}}\,. \tag{7}$$

From the Lagrange's mean value theorem, we have

$$r_k^\mathrm{s}(t) = \frac{\jmath k_0 \sqrt{P_\mathrm{T}}}{4\pi\sqrt{2R_\mathrm{L}}} \zeta \sum_{i=1}^{N_\mathrm{a}} \sum_{j=1}^{N_\mathrm{b}} \frac{\gamma_k^\mathrm{s}(\boldsymbol{p}_{ij}^\mathrm{L}) F_k^\mathrm{s}(\boldsymbol{p}_{ij}^\mathrm{L})}{\rho_\mathrm{T}(\boldsymbol{p}_{ij}^\mathrm{L})\rho_{\mathrm{R},k}(\boldsymbol{p}_{ij}^\mathrm{L})} \times e^{-\jmath k_0(\rho_\mathrm{T}(\boldsymbol{p}_{ij}^\mathrm{L})+\rho_{\mathrm{R},k}(\boldsymbol{p}_{ij}^\mathrm{L}))+\jmath\Phi_R(\breve{\boldsymbol{p}}_{ij}^\mathrm{L})} \tag{8}$$

where $\boldsymbol{p}_{ij}^\mathrm{L} = [(\breve{\boldsymbol{p}}_{ij}^\mathrm{L})^\mathrm{T}, 0]^\mathrm{T}$ and $\breve{\boldsymbol{p}}_{ij}^\mathrm{L} \in \mathcal{S}_{ij}$. Furthermore, we approximate $\boldsymbol{p}_{ij}^\mathrm{L}$ with the position $\boldsymbol{p}_{ij}$ of the (i, j) element of the $N_\mathrm{a} \times N_\mathrm{b}$ array. Then, we can get the signal model with a DIS for both near-field and far-field scenarios. The signal component $r_k^\mathrm{s}(t)$ is stated in Property 1.

Property 1: The signal component $r_k^\mathrm{s}(t)$ scattered by the agent-illuminated $N_\mathrm{a} \times N_\mathrm{b}$ DIS at the k-th anchor can be expressed as

$$r_k^\mathrm{s}(t) = \frac{\jmath k_0 \sqrt{P_\mathrm{T}}}{4\pi\sqrt{2R_\mathrm{L}}} \zeta \sum_{i=1}^{N_\mathrm{a}} \sum_{j=1}^{N_\mathrm{b}} \frac{\gamma_k^\mathrm{s}(\boldsymbol{p}_{ij}) F_k^\mathrm{s}(\boldsymbol{p}_{ij})}{\rho_\mathrm{T}(\boldsymbol{p}_{ij})\rho_{\mathrm{R},k}(\boldsymbol{p}_{ij})} \times e^{-\jmath k_0(\rho_\mathrm{T}(\boldsymbol{p}_{ij})+\rho_{\mathrm{R},k}(\boldsymbol{p}_{ij}))+\jmath\Phi_R(\breve{\boldsymbol{p}}_{ij})} \tag{9}$$

where ζ is the area of the DIS element. By ignoring the influence of polarization and directivity of the antennas and adding the far-field assumption, the discrete model can be reduced to the common signal model with the DIS in [49].

III. Integrated Localization and Communication Based on Continuous Intelligent Surfaces

This section considers the capability of CIS-aided communication with prior knowledge of the location of the receivers and transmitters, derives the Fisher information matrix (FIM) and Cramér-Rao lower bound (CRLB) for unknown agent position in general scenarios, and investigates a special case where the phase response function of the CIS is set to maximize the magnitude of the signal scattered by the CIS.

A. CIS-Aided Communication

With full knowledge of the location of transmitters and receivers, CISs can perform beamforming and improve the SNR of communication systems. Based on Proposition 1, the SNR at the k-th receiver of a CIS-aided communication system is given by

$$\mathrm{SNR}_k = \frac{1}{P_\mathrm{n} T_\mathrm{obs}} \int_0^{T_\mathrm{obs}} \left| r_k^\mathrm{s}(t) + \psi_k\, r_k^\mathrm{d}(t) \right|^2 dt \tag{10}$$

where the noise power P_n of a narrow-band system is given by

$$P_\mathrm{n} = \frac{N_0}{T_\mathrm{obs}}\,. \tag{11}$$

Furthermore, the spectral efficiency of the CIS-aided communications between the transmitter and the k-th receiver is found to be

$$C_k = \log_2 \left(1 + \frac{1}{N_0 B} \lim_{T\to\infty} \frac{1}{T} \int_0^T \left| r_k^\mathrm{s}(t) + \psi_k\, r_k^\mathrm{d}(t) \right|^2 dt \right) \tag{12}$$

where B is the bandwidth of the transmitted signal.

To maximize the spectral efficiency, we design the phase response function of the CIS with prior knowledge of the transmitter position and the receiver position as

$$\Phi_\mathrm{R}(\breve{\boldsymbol{p}}) = k_0 \big(\rho_{\mathrm{R},k}(\boldsymbol{p}) + \rho_\mathrm{T}(\boldsymbol{p})\big) - k_0 \rho_{\mathrm{D},k} - \arg\big(\gamma_k^\mathrm{s}(\boldsymbol{p}) F_k^\mathrm{s}(\boldsymbol{p})\big) + \arg\big(\gamma_k^\mathrm{d} F_k^\mathrm{d}\big) - \pi/2\,. \tag{13}$$

Under this condition, the phase response leads to a maximum modulus of r_k^s. Besides, the term $-k_0\rho_{\mathrm{D},k} - \arg\big(\gamma_k^\mathrm{s}(\boldsymbol{p}) F_k^\mathrm{s}(\boldsymbol{p})\big) + \arg\big(\gamma_k^\mathrm{d} F_k^\mathrm{d}\big)$ compensates for the phase difference between the scattered path and the direct path, leading to a maximum modulus of $r_k^\mathrm{s}(t) + r_k^\mathrm{d}(t)$. In the following, we refer to a CIS with this phase response function (13) as a focus-on-$\boldsymbol{p}_k$ CIS. From (5) and (12), notice that the spectral efficiency of communication aided by a focus-on-$\boldsymbol{p}_k$ CIS between the transmitter and the k-th receiver is a monotonically increasing function of the CIS size. Moreover, the spectral efficiency of CIS-aided communications configured by (13) is positively correlated with the carrier frequency f_c if the antenna size, transmitting power, and load resistance do not vary with f_c.

B. CIS-Aided Localization

To obtain the CRLB of the agent position estimation, we calculate the FIM, defined as [52]

$$\boldsymbol{J}(\boldsymbol{q}) = \mathbb{E}\left\{ \left[\frac{\partial}{\partial \boldsymbol{q}} \ln f(\boldsymbol{r}|\boldsymbol{q}) \right] \left[\frac{\partial}{\partial \boldsymbol{q}} \ln f(\boldsymbol{r}|\boldsymbol{q}) \right]^\mathrm{T} \right\} \tag{14}$$

where $f(\boldsymbol{r}|\boldsymbol{q})$ is the likelihood function of $\boldsymbol{q}$ when $\boldsymbol{r} = [r_1, r_2, \ldots, r_K]^\mathrm{T}$ is observed. Due to the independence of propagations to different anchors, the likelihood function can be written as

$$f(\boldsymbol{r}|\boldsymbol{q}) = \prod_{k=1}^{K} f(r_k|\boldsymbol{q})\,. \tag{15}$$

Authorized licensed use limited to: MIT Libraries. Downloaded on June 19,2022 at 19:18:15 UTC from IEEE Xplore. Restrictions apply.

All the information contained in all measurements of the anchors contributes to a bound for the agent position. The bound on the mean-square error (MSE) of the estimator can be calculated by the measurements obtained based on either centralized estimators or distributed estimators.

Proposition 2: Based on the signal model in Proposition 1, the FIM of the agent position $\boldsymbol{q}$ can be written as

$$\boldsymbol{J}(\boldsymbol{q}) = \sum_{k=1}^{K} \boldsymbol{J}_k(\boldsymbol{q}) \tag{16}$$

where $\boldsymbol{J}_k(\boldsymbol{q})$ is the contribution of the k-th anchor, given by

$$\begin{aligned}\boldsymbol{J}_k(\boldsymbol{q}) = \frac{P_\mathrm{T}}{2P_\mathrm{n}R_\mathrm{L}} \Re\Big\{ &\big[\boldsymbol{\mu}_k^\mathrm{s} + \boldsymbol{\sigma}_k^\mathrm{s} + \psi_k(\boldsymbol{\mu}_k^\mathrm{d} + \boldsymbol{\sigma}_k^\mathrm{d})\big] \\ &\times \big[\boldsymbol{\mu}_k^\mathrm{s} + \boldsymbol{\sigma}_k^\mathrm{s} + \psi_k(\boldsymbol{\mu}_k^\mathrm{d} + \boldsymbol{\sigma}_k^\mathrm{d})\big]^\mathrm{H}\Big\}\end{aligned} \tag{17}$$

where

$$\begin{aligned}\boldsymbol{\mu}_k^\mathrm{s} &= \frac{\jmath k_0}{2\pi}\int_\mathcal{S} \gamma_k^{\mathrm{s}*}(\boldsymbol{p}) F_k^{\mathrm{s}*}(\boldsymbol{p}) \frac{e^{\jmath k_0 \rho_{\mathrm{R},k}(\boldsymbol{p})}}{\rho_{\mathrm{R},k}(\boldsymbol{p})} \frac{e^{\jmath k_0 \rho_\mathrm{T}(\boldsymbol{p})}}{\rho_\mathrm{T}(\boldsymbol{p})^2} \\ &\quad\times \Big(-\jmath k_0 + \frac{1}{\rho_\mathrm{T}(\boldsymbol{p})}\Big) e^{-\jmath \Phi_\mathrm{R}(\breve{\boldsymbol{p}})} (\boldsymbol{q}-\boldsymbol{p})\, d\breve{\boldsymbol{p}} && \text{(18a)} \\ \boldsymbol{\mu}_k^\mathrm{d} &= \gamma_k^{\mathrm{d}*} F_k^{\mathrm{d}*} \frac{e^{\jmath k_0 \rho_{\mathrm{D},k}}}{(\rho_{\mathrm{D},k})^2} \Big(\jmath k_0 - \frac{1}{\rho_{\mathrm{D},k}}\Big)(\boldsymbol{q}-\boldsymbol{p}_k) && \text{(18b)} \\ \boldsymbol{\sigma}_k^\mathrm{s} &= \frac{-\jmath k_0}{2\pi}\int_\mathcal{S} \frac{e^{\jmath k_0 \rho_\mathrm{T}(\boldsymbol{p})}}{\rho_\mathrm{T}(\boldsymbol{p})} \frac{e^{\jmath k_0 \rho_{\mathrm{R},k}(\boldsymbol{p})}}{\rho_{\mathrm{R},k}(\boldsymbol{p})} \\ &\quad\times\ e^{-\jmath \Phi_\mathrm{R}(\breve{\boldsymbol{p}})} \frac{\partial}{\partial \boldsymbol{q}} \big(\gamma_k^{\mathrm{s}*}(\boldsymbol{p}) F_k^{\mathrm{s}*}(\boldsymbol{p})\big)\, d\breve{\boldsymbol{p}} && \text{(18c)} \\ \boldsymbol{\sigma}_k^\mathrm{d} &= \frac{e^{\jmath k_0 \rho_{\mathrm{D},k}}}{\rho_{\mathrm{D},k}} \frac{\partial}{\partial \boldsymbol{q}} \big(\gamma_k^{\mathrm{d}*} F_k^{\mathrm{d}*}\big)\,. && \text{(18d)}\end{aligned}$$

Moreover, the MSE of any unbiased estimator $\hat{\mathbf{q}}$ of the agent position satisfies

$$\mathbb{E}\big\{(\hat{\mathbf{q}} - \boldsymbol{q})(\hat{\mathbf{q}} - \boldsymbol{q})^\mathrm{T}\big\} \succcurlyeq \boldsymbol{J}(\boldsymbol{q})^{-1} \tag{19}$$

where the right hand side is called the CRLB [38].

Proof: The proof follows from straightforward calculation of (14).

Remark 3: The FIM $\boldsymbol{J}_k(\boldsymbol{q})$ is generally a rank-2 real matrix. Specifically, $\boldsymbol{\mu}_k^\mathrm{s}$ and $\boldsymbol{\sigma}_k^\mathrm{s}$ are determined by the position of the agent relative to the CIS, and $\boldsymbol{\mu}_k^\mathrm{d}$ and $\boldsymbol{\sigma}_k^\mathrm{d}$ are determined by the position of the agent relative to the k-th anchor. When the influence of the directivity and polarization of the antennas can be neglected, the vectors $\boldsymbol{\sigma}_k^\mathrm{s}$ and $\boldsymbol{\sigma}_k^\mathrm{d}$ become zero vectors, and the FIM at the k-th anchor is reduced to

$$\boldsymbol{J}_k(\boldsymbol{q}) = \frac{P_\mathrm{T}}{2P_\mathrm{n}R_\mathrm{L}} \Re\left\{(\boldsymbol{\mu}_k^\mathrm{s} + \boldsymbol{\mu}_k^\mathrm{d})(\boldsymbol{\mu}_k^\mathrm{s} + \boldsymbol{\mu}_k^\mathrm{d})^\mathrm{H}\right\} \tag{20}$$

whose rank remains 2 in general.

C. Case Study: CISs With Focusing Control

To clarify the relationship between position information and system parameters, additional assumptions are made to simplify the expressions for the case of interest. We assume that λ_0 is significantly smaller than $\rho_\mathrm{T}(\boldsymbol{p})$ and $\rho_{\mathrm{D},k}$, i.e., (A3) $\lambda_0 \ll \rho_\mathrm{T}(\boldsymbol{p})$ and (A4) $\lambda_0 \ll \rho_{\mathrm{D},k}$.

With (A3), we have

$$\begin{aligned}\boldsymbol{\mu}_k^\mathrm{s} \approx \frac{k_0^2}{2\pi}\int_\mathcal{S} &\gamma_k^{\mathrm{s}*}(\boldsymbol{p}) F_k^{\mathrm{s}*}(\boldsymbol{p}) \\ &\times \frac{e^{\jmath k_0 \rho_{\mathrm{R},k}(\boldsymbol{p})}}{\rho_{\mathrm{R},k}(\boldsymbol{p})} \frac{e^{\jmath k_0 \rho_\mathrm{T}(\boldsymbol{p})}}{\rho_\mathrm{T}(\boldsymbol{p})^2} e^{-\jmath \Phi_\mathrm{R}(\breve{\boldsymbol{p}})} (\boldsymbol{q}-\boldsymbol{p})\, d\breve{\boldsymbol{p}}\,.\end{aligned} \tag{21}$$

Meanwhile, with (A4), we have

$$\boldsymbol{\mu}_k^\mathrm{d} \approx \jmath k_0 \gamma_k^{\mathrm{d}*} F_k^{\mathrm{d}*} \frac{e^{\jmath k_0 \rho_{\mathrm{D},k}}}{(\rho_{\mathrm{D},k})^2} (\boldsymbol{q}-\boldsymbol{p}_k)\,. \tag{22}$$

For the agent and the anchors with same dipole antennas along the z-axis, we can obtain the FIM for a focus-on-$\boldsymbol{p}_k$ CIS as shown in Proposition 3.

Proposition 3: With (A1)-(A4), the FIM of a focus-on-$\boldsymbol{p}_k$ CIS at the k-th anchor with small dipole antennas whose length is Δz along the z-axis is given by

$$\boldsymbol{J}_k(\boldsymbol{q}) = \boldsymbol{J}_k^\mathrm{s}(\boldsymbol{q}) + \psi_k\left(\boldsymbol{J}_k^\mathrm{d}(\boldsymbol{q}) + \boldsymbol{C}_k(\boldsymbol{q})\right) \tag{23}$$

where $\boldsymbol{J}_k^\mathrm{s}(\boldsymbol{q})$, $\boldsymbol{J}_k^\mathrm{d}(\boldsymbol{q})$, and $\boldsymbol{C}_k(\boldsymbol{q})$ represent the information from the scattering path, the direct path, and the coupling of the two paths, respectively, given by

$$\begin{aligned}\boldsymbol{J}_k^\mathrm{s}(\boldsymbol{q}) &= \frac{3\pi\eta_0 P_\mathrm{T}(\Delta z)^2 f_\mathrm{c}^4}{8P_\mathrm{n}R_\mathrm{L}c_0^4}\, \boldsymbol{u}_k^\mathrm{s}(\boldsymbol{u}_k^\mathrm{s})^\mathrm{T} && \text{(24a)} \\ \boldsymbol{J}_k^\mathrm{d}(\boldsymbol{q}) &= \frac{3\pi\eta_0 P_\mathrm{T}(\Delta z)^2 f_\mathrm{c}^2}{8P_\mathrm{n}R_\mathrm{L}c_0^2}\, \boldsymbol{u}_k^\mathrm{d}(\boldsymbol{u}_k^\mathrm{d})^\mathrm{T} && \text{(24b)} \\ \boldsymbol{C}_k(\boldsymbol{q}) &= \frac{3\pi\eta_0 P_\mathrm{T}(\Delta z)^2 f_\mathrm{c}^3}{64P_\mathrm{n}R_\mathrm{L}c_0^3}\left(\boldsymbol{u}_k^\mathrm{s}(\boldsymbol{u}_k^\mathrm{d})^\mathrm{T} + \boldsymbol{u}_k^\mathrm{d}(\boldsymbol{u}_k^\mathrm{s})^\mathrm{T}\right). && \text{(24c)}\end{aligned}$$

Here $\boldsymbol{u}_k^\mathrm{s}, \boldsymbol{u}_k^\mathrm{d} \in \mathbb{R}^3$ are determined by the position of CIS, agent and anchors and the size and shape of CIS, i.e., $\boldsymbol{q}$, $\boldsymbol{p}_k$, and $\mathcal{S}$, expressed as (55) and (56).

Proof: See Appendix C.

Remark 4: The FIM consists of three components: the FIM from the scattering path, the FIM from the direct path, and the FIM from the coupling of the two paths, which means that, if the CIS is removed, then $\boldsymbol{J}_k(\boldsymbol{q}) = \boldsymbol{J}_k^\mathrm{d}(\boldsymbol{q})$ and if the direct path is obstructed, then $\boldsymbol{J}_k(\boldsymbol{q}) = \boldsymbol{J}_k^\mathrm{s}(\boldsymbol{q})$. To reveal the benefit only from the CIS as f_c increases but not from the agent and the anchors, we consider that the antenna size is proportional to the wavelength, and thus the benefit from the dipole antennas of the agent and the anchors is eliminated. In this case, $\boldsymbol{J}_k^\mathrm{s}(\boldsymbol{q})$ is approximately proportional to f_c^2 at high signal frequency, which is fully contributed by the CIS with dynamic focusing control due to the conformed scattering via the CIS. If the transmitting power and the antenna size are constant, $\boldsymbol{J}_k^\mathrm{s}(\boldsymbol{q})$ is approximately proportional to f_c^4, which implies that the introduction of the CIS can largely improve the performance of the localization system at high signal frequency.

Remark 5: By setting the phase response function in (13), the increase in the received signal power results in the optimal FIM at the k-th anchor. Although the phase response function (13) requires knowledge of the agent position, the configuration can be achieved in an iterative way. The initial phase response of the CIS is configured randomly and a rough estimation of the agent position is acquired. Substituting the rough estimation of the agent position into (13), we obtain a

Authorized licensed use limited to: MIT Libraries. Downloaded on June 19,2022 at 19:18:15 UTC from IEEE Xplore. Restrictions apply.

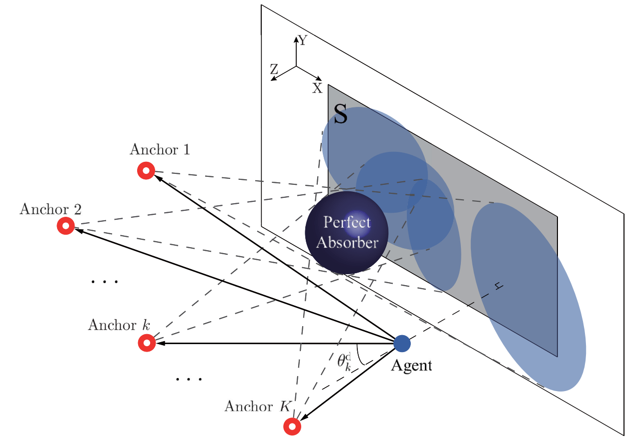

Fig. 2. Localization with an OSP. The intersections of the CIS and translucent-blue regions on the X-Y plane are invalid zones for the anchors. The OSPs are modeled as perfect absorbers.

finer estimation of the agent position. After multiple iterations, the phase response of the CIS can be configured. It is worthy to note that an optimal FIM results in higher localization accuracy, which leads to better performance of CIS-aided communication. Therefore, a CIS-aided localization system and a CIS-aided communication system can be integrated as a CIS-aided ISAC system and jointly optimized.

IV. CIS-Aided Localization With Obstacles on the Scattering Paths and Additional CISs

This section extends the CIS-aided localization systems with obstacles on the scattering paths (OSPs) and additional CISs.

A. Localization With Obstacles on the Scattering Paths

Consider an OSP as a perfect absorber, as shown in Fig. 2. The OSP can obstruct some of the scattering paths and the EM waves scattered to the OSP are perfectly absorbed. Here, we make a simple assumption on that the EM waves scattered on the OSP are so weak after reflection that they can be neglected. Besides, we assume that the size of the OSP is much larger than the wavelength of the EM waves, thus the diffraction is not accounted. For a range-based localization system that relies on the direct path, once a perfect absorber is on the direct path, the receiver will be covered in the shadow caused by the absorber and hardly receive the signals from the transmitter. However, with the aid of a CIS whose area is large enough, the absorber cannot obstruct all the EM waves scattered by the CIS. Therefore, the intensity of the position information is still significant even though it is reduced by the presence of OSPs.

For the k-th anchor, an OSP creates an invalid zone on the CIS as shown in Definition 1.

Definition 1 (Invalid zone on CISs): For the k-th anchor, the invalid zone $\mathcal{B}_k$ on a CIS is defined as

$$\mathcal{B}_k = \big\{\boldsymbol{p} \in \mathcal{S}_{\text{eff}} | \text{the straight line determined by } \boldsymbol{p}_k \text{ and } \boldsymbol{p} \\ \cap \text{ the space occupied by the OSPs} \neq \varnothing \big\} \quad (25)$$

where $\mathcal{S}_{\text{eff}}$ denotes the area of the CIS illuminated by the agent.

The EM waves scattered on the invalid zone cannot reach the corresponding anchor. Therefore, the phase response on the invalid zone of the CIS is irrelevant to the corresponding anchor.

Corollary 1: The FIM of the k-th anchor when there are OSPs is given by

$$\boldsymbol{J}_k^{\text{O}}(\boldsymbol{q}) = \frac{P_{\text{T}}}{2P_{\text{n}}R_{\text{L}}} \Re\Big\{ \big[\boldsymbol{\mu}_k^{\text{s,o}} + \boldsymbol{\sigma}_k^{\text{s,o}} + \psi_k(\boldsymbol{\mu}_k^{\text{d}} + \boldsymbol{\sigma}_k^{\text{d}})\big] \\ \times \big[\boldsymbol{\mu}_k^{\text{s,o}} + \boldsymbol{\sigma}_k^{\text{s,o}} + \psi_k(\boldsymbol{\mu}_k^{\text{d}} + \boldsymbol{\sigma}_k^{\text{d}})\big]^{\text{H}} \Big\} \quad (26)$$

where

$$\boldsymbol{\mu}_k^{\text{s,o}} = \frac{\jmath k_0}{2\pi} \int_{\mathcal{S}_{\text{eff}} \backslash \mathcal{B}_k} \gamma_k^{\text{s}*}(\boldsymbol{p}) F_k^{\text{s}*}(\boldsymbol{p}) \frac{e^{\jmath k_0 \rho_{\text{R},k}(\boldsymbol{p})}}{\rho_{\text{R},k}(\boldsymbol{p})} \frac{e^{\jmath k_0 \rho_{\text{T}}(\boldsymbol{p})}}{\rho_{\text{T}}(\boldsymbol{p})^2} \\ \times \Big(-\jmath k_0 + \frac{1}{\rho_{\text{T}}(\boldsymbol{p})} \Big) e^{-\jmath \Phi_{\text{R}}(\breve{\boldsymbol{p}})} (\boldsymbol{q} - \boldsymbol{p})\, d\breve{\boldsymbol{p}} \quad (27a)$$

$$\boldsymbol{\sigma}_k^{\text{s,o}} = \frac{-\jmath k_0}{2\pi} \int_{\mathcal{S}_{\text{eff}} \backslash \mathcal{B}_k} \frac{e^{\jmath k_0 \rho_{\text{T}}(\boldsymbol{p})}}{\rho_{\text{T}}(\boldsymbol{p})} \frac{e^{\jmath k_0 \rho_{\text{R},k}(\boldsymbol{p})}}{\rho_{\text{R},k}(\boldsymbol{p})} \\ \times\ e^{-\jmath \Phi_{\text{R}}(\breve{\boldsymbol{p}})} \frac{\partial}{\partial \boldsymbol{q}} \big(\gamma_k^{\text{s}*}(\boldsymbol{p}) F_k^{\text{s}*}(\boldsymbol{p})\big)\, d\breve{\boldsymbol{p}}\,. \quad (27b)$$

Proof: Straightforward results from Proposition 2.

Remark 6: The recognition of every invalid zone on the CIS can optimize the phase response of the CIS further. Furthermore, if a localization system has multiple anchors, the invalid zone of one anchor may be out of the invalid zone of another anchor. Therefore, though the invalid zone $\mathcal{B}_k$ is unable to benefit the k-th anchor, this invalid zone can serve other accessible anchors and improve the performance of the system. In other words, for a problem of phase response optimization of the whole CIS, it can be divided into sub-problems that optimize the phase response on the domain formed by the intersection and difference set of $\mathcal{B}_k$, $k = 1, 2, \ldots, K$ and $\mathcal{S}_{\text{eff}}$. In particular, the phase response function can be set as

$$\Phi_{\text{R}}(\breve{\boldsymbol{p}}) = \begin{cases} k_0\big(\rho_{\text{R},k}(\boldsymbol{p}) + \rho_{\text{T}}(\boldsymbol{p})\big) - k_0 \rho_{\text{D},k} + \arg\big(\gamma_k^{\text{d}} F_k^{\text{d}}\big) \\ \quad - \arg\big(\gamma_k^{\text{s}}(\boldsymbol{p}) F_k^{\text{s}}(\boldsymbol{p})\big) - \pi/2, \quad \breve{\boldsymbol{p}} \in \bigcup\limits_{m=1}^{k} \mathcal{S}_{\text{eff}} \backslash \mathcal{B}_m \\ 0, \qquad \breve{\boldsymbol{p}} \in \bigcap\limits_{k=1}^{K} \mathcal{B}_k \end{cases} \quad (28)$$

where the sequence $k = 1, 2, \ldots, K$ represents the priority of the anchor, and the anchor with a larger subscript has higher priority to be served by the CIS. Here, the phase response function is set to zero in $\bigcap_{k=1}^{K} \mathcal{B}_k$ to eliminate the ambiguity when $\bigcap_{k=1}^{K} \mathcal{B}_k \neq \varnothing$. In addition, it is feasible for the CIS to obtain perfect knowledge of the OSP in the configuration step when the CIS has elements for sensing. The invalid zones can be determined based on the way in which the anchors illuminate the sensing elements embedded on the CIS in a specific sequence. Furthermore, the CIS can be configured in a similar method as in Remark 5.

The signals scattered twice by OSPs have low signal strength and thus can be omitted. As shown in case (2)

Authorized licensed use limited to: MIT Libraries. Downloaded on June 19,2022 at 19:18:15 UTC from IEEE Xplore. Restrictions apply.

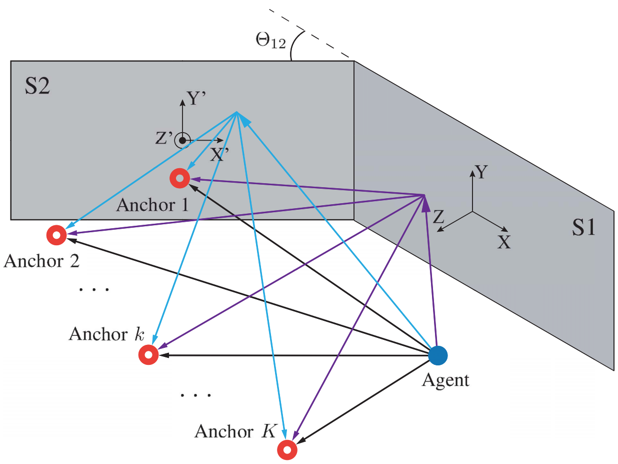

Fig. 3. Localization with two CISs. Here the angle between the two CISs is Θ_{12}, and the second-scattered EM waves are neglected because of their low strength.

of Fig. 5, even the signals scattered once in a semi-infinite space by a large scattering plane have low SNR, not to say OSPs that scatter the signals to all directions. In the configuration (28), the EM waves scattered coherently to the anchors can avoid the interference of the OSP, and thus the scattering effect of OSPs is weakened further. The diffraction effect is not considered in the modeling of the obstacles, since wavelength-size obstacles are uncommon in high-frequency scenarios. Therefore, modeling OSPs as perfect absorbers is appropriate for the considered high-frequency scenarios.

B. Localization With Multiple CISs

Consider a localization system with multiple CISs, where the second-scattered EM waves are neglected due to their low strength. In these scenarios, we focus on what an additional CIS introduces, and to what extent the relative position of the CISs affect the performance limit of the entire system. Without loss of generality, a localization system with two nonparallel CISs is considered, as shown in Fig. 3; an extension to a localization system with multiple CISs is straightforward.

Corollary 2: In a localization system with CISs Sm, $m = 1, 2, \ldots M$, the FIM from the k-th anchor is given by

$$\boldsymbol{J}_k^{\mathrm{M}}(\boldsymbol{q}) = \frac{P_{\mathrm{T}}}{2P_{\mathrm{n}}R_{\mathrm{L}}}\Re\Bigg\{\Bigg[\sum_{m=1}^{M}(\boldsymbol{\mu}_k^{\mathrm{s},m}+\boldsymbol{\sigma}_k^{\mathrm{s},m}) + \psi_k(\boldsymbol{\mu}_k^{\mathrm{d}}+\boldsymbol{\sigma}_k^{\mathrm{d}})\Bigg] \times\Bigg[\sum_{m=1}^{M}(\boldsymbol{\mu}_k^{\mathrm{s},m}+\boldsymbol{\sigma}_k^{\mathrm{s},m}) + \psi_k(\boldsymbol{\mu}_k^{\mathrm{d}}+\boldsymbol{\sigma}_k^{\mathrm{d}})\Bigg]^{\mathrm{H}}\Bigg\} \tag{29}$$

where

$$\begin{aligned}\boldsymbol{\mu}_k^{\mathrm{s},m} = \frac{k_0}{2\pi\jmath}\int_{\mathcal{S}_m} & \gamma_k^{\mathrm{s}*}(\boldsymbol{R}_m\boldsymbol{p}+\boldsymbol{p}_{\mathrm{S}m})F_k^{\mathrm{s}*}(\boldsymbol{R}_m\boldsymbol{p}+\boldsymbol{p}_{\mathrm{S}m}) \\ &\times \frac{e^{\jmath k_0\rho_{\mathrm{R,k}}(\boldsymbol{R}_m\boldsymbol{p}+\boldsymbol{p}_{\mathrm{S}m})}}{\rho_{\mathrm{R,k}}(\boldsymbol{R}_m\boldsymbol{p}+\boldsymbol{p}_{\mathrm{S}m})}\frac{e^{\jmath k_0\rho_{\mathrm{T}}(\boldsymbol{R}_m\boldsymbol{p}+\boldsymbol{p}_{\mathrm{S}m})}}{\rho_{\mathrm{T}}(\boldsymbol{R}_m\boldsymbol{p}+\boldsymbol{p}_{\mathrm{S}m})^2} \\ &\times\left(-\jmath k_0+\frac{1}{\rho_{\mathrm{T}}(\boldsymbol{R}_m\boldsymbol{p}+\boldsymbol{p}_{\mathrm{S}m})}\right)e^{-\jmath\Phi_{\mathrm{R},m}(\breve{\boldsymbol{p}})} \\ &\times\left(\boldsymbol{q}-(\boldsymbol{R}_m\boldsymbol{p}+\boldsymbol{p}_{\mathrm{S}m})\right)d\breve{\boldsymbol{p}}\end{aligned} \tag{30a}$$

$$\begin{aligned}\boldsymbol{\sigma}_k^{\mathrm{s},m} = \frac{\jmath k_0}{2\pi}\int_{\mathcal{S}_m} & \frac{e^{\jmath k_0\rho_{\mathrm{T}}(\boldsymbol{R}_m\boldsymbol{p}+\boldsymbol{p}_{\mathrm{S}m})}}{\rho_{\mathrm{T}}(\boldsymbol{R}_m\boldsymbol{p}+\boldsymbol{p}_{\mathrm{S}m})}\frac{e^{\jmath k_0\rho_{\mathrm{R,k}}(\boldsymbol{R}_m\boldsymbol{p}+\boldsymbol{p}_{\mathrm{S}m})}}{\rho_{\mathrm{R,k}}(\boldsymbol{R}_m\boldsymbol{p}+\boldsymbol{p}_{\mathrm{S}m})} \\ &\times\frac{\partial}{\partial\boldsymbol{q}}\left(\gamma_k^{\mathrm{s}*}(\boldsymbol{R}_m\boldsymbol{p}+\boldsymbol{p}_{\mathrm{S}m})F_k^{\mathrm{s}*}(\boldsymbol{R}_m\boldsymbol{p}+\boldsymbol{p}_{\mathrm{S}m})\right) \\ &\times e^{-\jmath\Phi_{\mathrm{R},m}(\breve{\boldsymbol{p}})}\,d\breve{\boldsymbol{p}}\end{aligned} \tag{30b}$$

in which $\mathcal{S}_m$ is the set of two-dimensional coordinates of all points on the m-th CIS; $\boldsymbol{R}_m$ and $\boldsymbol{p}_{\mathrm{S}m}$ are the rotation matrix describing the rotation of the m-th CIS and the relative position of the m-th CIS, respectively.

Proof: See Appendix D.

Remark 7: The phase response of the m-th CIS can be set to focus on the k-th anchor as

$$\begin{aligned}\Phi_{\mathrm{R},m}(\breve{\boldsymbol{p}}) = k_0&\left(\rho_{\mathrm{R},k}(\boldsymbol{R}_m\boldsymbol{p}+\boldsymbol{p}_{\mathrm{S}m})+\rho_{\mathrm{T}}(\boldsymbol{R}_m\boldsymbol{p}+\boldsymbol{p}_{\mathrm{S}m})\right) \\ &-\arg\left(\gamma_k^{\mathrm{s}}(\boldsymbol{R}_m\boldsymbol{p}+\boldsymbol{p}_{\mathrm{S}m})F_k^{\mathrm{s}}(\boldsymbol{R}_m\boldsymbol{p}+\boldsymbol{p}_{\mathrm{S}m})\right) \\ &-k_0\rho_{\mathrm{D},k}+\arg(\gamma_k^{\mathrm{d}}F_k^{\mathrm{d}})-\pi/2.\end{aligned} \tag{31}$$

This configuration can be achieved in a similar method proposed in Remark 5.

Generally, Corollary 2 assumes that each CIS is not set on the path between the anchors or agents and other CISs, and the assumption of CISs deployment can be easily met. For example, for a cubic room, CISs deployed on the ceiling and walls hardly violate the assumption. It is worthy to note that if a CIS is obstructed by other CISs in a localization system with multiple CISs, Corollary 2 does not hold. However, we can view other CISs as obstacles for the CIS and acquire the FIM from Corollary 1.

With the aid of CISs, the scattered signals can be directed to favorable directions. Due to the power concentration on the favorable direction, the power scattered by the CIS to other direction is significantly weakened, compared with power scattered by scattering planes. The directionality of CISs is enhanced as the carrier frequency increases, so the power scattered by the CIS to other direction will be reduced further if the carrier frequency increases. In addition, it will be seen in Fig. 5 that the signal scattered by a scattering plane is much weaker than the signal scattered by the CIS at a specific direction. Therefore, multi-bounce scatterings between multiple CISs can be neglected.

V. Numerical Results and Discussion

This section simulates four scenarios to evaluate the performance of integrated localization and communication systems under different parameters, the performance of localization with OSPs, and the performance of localization with multiple planes including CISs and scattering planes.

The considered localization and communication systems have 3 anchors and 1 agent with dipole antennas along the z-axis, and the agent communicates with the anchors. We set the bandwidth of the transmitted signals as 3 MHz, the simulation step on the square-shape $D \times D$ planes including DISs, CISs, and the scattering planes as $\lambda_0/5 \times \lambda_0/5$, the parameters of dipole antenna along z-axis of the agent and the anchors as $P_{\mathrm{T}} = 10\,\mathrm{mW}$ and $\Delta z = \lambda_0/2$. The noise figure and temperature are set as 5 dB and room temperature, respectively. The positions of the anchors are $\boldsymbol{p}_1 = (30, 20, 300)$, $\boldsymbol{p}_2 = (150, 0, 300)$, and $\boldsymbol{p}_3 = (150, 0, 310)$, respectively. The agent $\boldsymbol{q}$ is in the space of $[18, 22] \times [28, 32] \times [28, 32]$. The unit of

Authorized licensed use limited to: MIT Libraries. Downloaded on June 19,2022 at 19:18:15 UTC from IEEE Xplore. Restrictions apply.

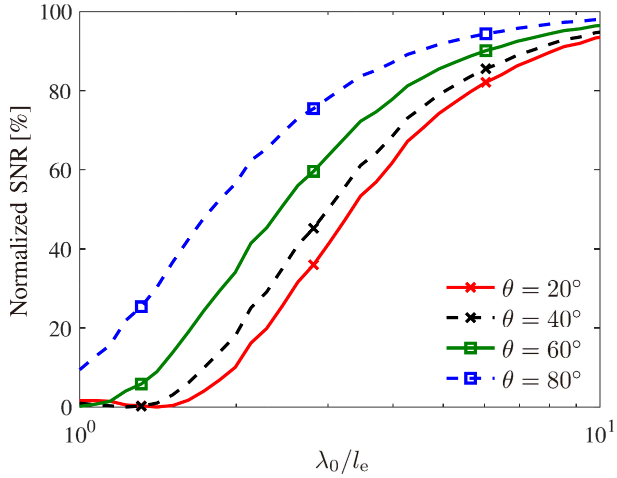

Fig. 4. SNR of DIS-aided communication normalized by that of CIS-aided communication at different directions where the receiver is deployed.

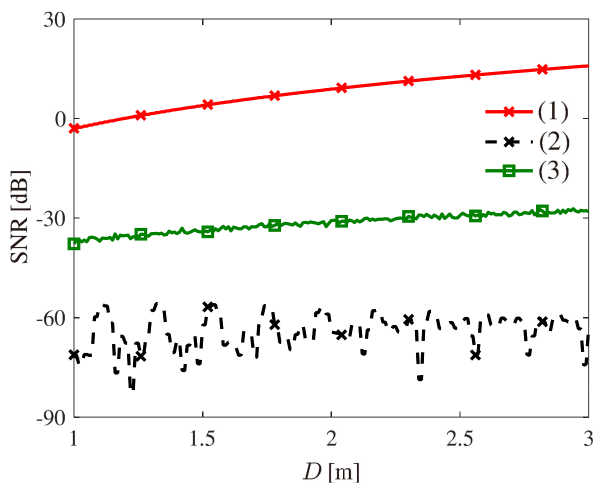

Fig. 5. Performance comparison of communication aided by (1) focus-on-$\boldsymbol{p}_2$ CIS (2) scattering plane (3) random-configured CIS.

the coordinates of the anchors and the agent positions is meter. In the simulations related to localization, 100 realizations of agent position are used to determine the average root squared position error bound (SPEB), where SPEB is the trace of CRLB introduced in Proposition 2 [24].

A. CIS-Aided Communication Under Different Parameters

To show the difference between CIS and DISs with different spacing of element l_e, we evaluate an RIS-aided communication system whose transmitter is at $(20, 20, 30)$ (m) and the receiver is at $(200\cos\theta, 0, 200\sin\theta)$ (m), and the direct path between the transmitter and the receiver is obstructed. The size D of the CISs is set to 3 m, and the carrier frequency is set to 3 GHz. The normalized SNR refers to SNR of DIS-aided communication normalized by that of CIS-aided communication. A DIS with elements larger than the wavelength cannot affect incidence waves effectively, thus we consider $\lambda_0/l_e > 1$. Fig. 4 shows that when the spacing of elements on DIS is below $\lambda_0/4$, i.e., $\lambda_0/l_e \geqslant 4$, the performance of DISs when $\theta = 20°$ exceeds 90% SNR of CIS. As the spacing of elements on DIS decreases, the performance of DIS-aided communication increases and approaches the performance of CIS-aided communication.

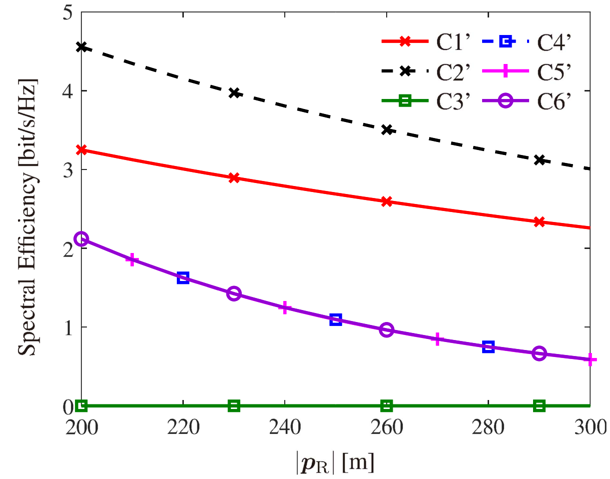

Fig. 6. Spectral efficiency as a function of the distance between the receiver and the CIS for different case studies.

TABLE II
A NOTATION OF SCENARIO 1'

Cases	ODP	Plane Type
C1'	1	1 focus-on-$\boldsymbol{p}_R$ CIS given by (13)
C2'	0	1 focus-on-$\boldsymbol{p}_R$ CIS given by (13)
C3'	1	1 Scattering plane
C4'	0	1 Scattering plane
C5'	0	None
C6'	0	1 random-configured CIS

To quantify the gain brought by CIS on the SNR, we study the communication between the receiver and the transmitter whose direct path is obstructed. Specifically, we compare the communication aided by a focus-on-$\boldsymbol{p}_2$ CIS, a scattering plane, and a random-configured CIS, respectively. The transmitter is at $(20, 20, 30)$ (m). Here, a scattering plane refers to a plane whose phase response is zero, and a random-configured CIS refers to a plane whose phase response follows a uniform distribution in $[0, 2\pi)$. The size D of the planes is set as 3 m, and the carrier frequency is set as 3 GHz. Fig. 5 shows that the SNR of CIS-aided communication is enhanced significantly from around -3 dB to around 15 dB as the size of the CIS increases, while the SNR for communication aided by a scattering plane and the average SNR for communication aided by random-configured CIS remain unchanged around -60 and -30 dB, respectively. This is because the signal scattered by a focus-on-$\boldsymbol{p}_2$ CIS is superimposed coherently at the receiver.

To further explore the theoretical limit of CIS-aided communications, six cases with and without an obstacle on the direct path (ODP) are considered as listed in Table II, and the receiver is at $\boldsymbol{p}_R = |\boldsymbol{p}_R|(\cos\theta,\ 0,\ \sin\theta)$. In Fig. 6, the carrier frequency is 3 GHz, $\theta = 120°$, and the size D of the CIS or the scattering plane is 3 m. Fig. 6 shows that with the aid of a focus-on-$\boldsymbol{p}_R$ CIS, the spectral efficiency is more than twice higher than that without the aid of a CIS. Fig. 6 also shows that the performance gains in spectral efficiency provided by a random-configured CIS and a scattering plane are smaller compared with that provided by a focus-on-$\boldsymbol{p}_R$ CIS.

In Fig. 7, the carrier frequency of the localization systems varies from 1 GHz to 30 GHz, and the size of the antenna is

Authorized licensed use limited to: MIT Libraries. Downloaded on June 19,2022 at 19:18:15 UTC from IEEE Xplore. Restrictions apply.

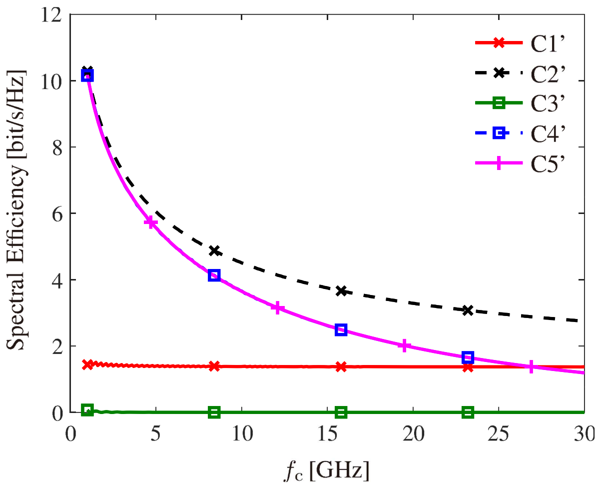

Fig. 7. Impact on spectral efficiency of CIS-aided communications from the carrier frequency.

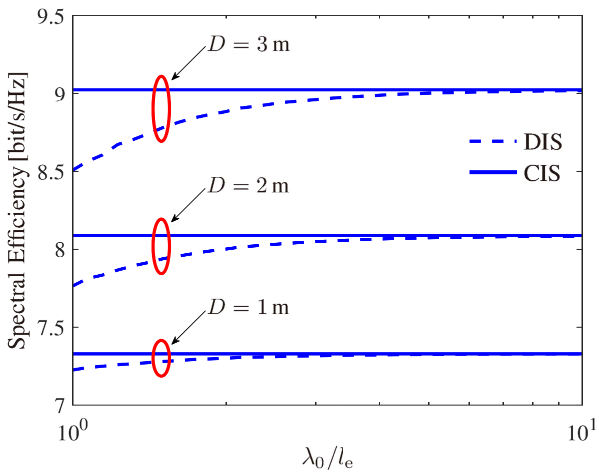

Fig. 8. Impact on spectral efficiency of RIS-aided communications from the size of RISs and the spacing element of the DISs.

$\lambda_0/2$. The size of the CIS and scattering planes are set as $D = 1\,\mathrm{m}$, and $|\boldsymbol{p}_\mathrm{R}|$ and θ are set as $200\,\mathrm{m}$ and $120°$, respectively. Fig. 7 shows that the spectral efficiency provided by the direct path decreases as the carrier frequency increases, and it is because the aperture of the Rx antenna is proportional to λ_0^2. Fig. 7 also shows that the performance gain in the spectral efficiency with the aid of a focus-on-$\boldsymbol{p}_\mathrm{R}$ CIS is significant compared with that without the aid of a CIS, especially when the carrier frequency is high. Moreover, with the aid of a CIS, spectral efficiency keeps unchanged as the frequency increases, and it is because the gain provided by the CIS compensates for the deterioration caused by the reduced aperture of the Rx antenna.

In Fig. 8, we consider cases without ODPs aided by RISs. The carrier frequency is $3\,\mathrm{GHz}$, and $|\boldsymbol{p}_\mathrm{R}|$ and θ are set as $200\,\mathrm{m}$ and $120°$, respectively. Fig. 8 shows that the spectral efficiency is enhanced as the RIS size increases. This is because the RIS collects more power with a larger size. Fig. 8 also shows that the spectral efficiency of DIS-aided communications approaches that of CIS-aided communications as the spacing of DIS elements decreases. Better gains of CISs over DISs can be expected in scenarios with multiple receivers, due to the ability of CISs to form radiation patterns with higher directivity.

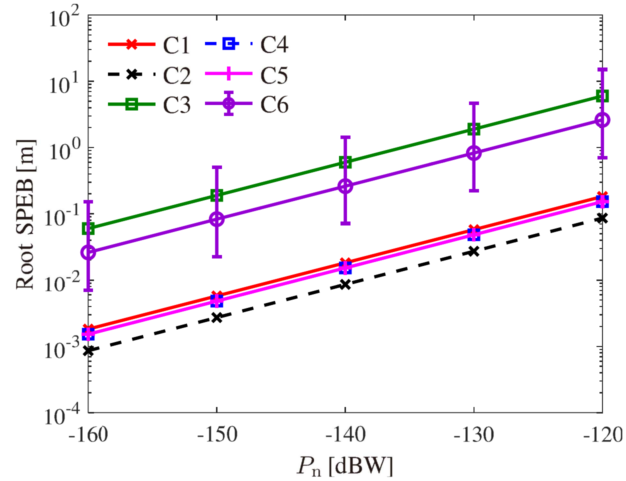

Fig. 9. Localization accuracy comparison among 6 different cases in Scenario 1.

TABLE III

A NOTATION OF SCENARIO 1

Cases	ODP	Plane Type
C1	1	1 focus-on-$\boldsymbol{p}_1$ CIS given by (13)
C2	0	1 focus-on-$\boldsymbol{p}_1$ CIS given by (13)
C3	1	1 Scattering plane
C4	0	1 Scattering plane
C5	0	None
C6	1	1 random-configured CIS

B. CIS-Aided Localization Under Different Parameters

To show the enhancement of the CIS in localization, we consider the Scenario 1 with and without an ODP between the agent and the anchor. In this scenario, six different cases are considered as listed in Table III. In particular, cases C3 and C5 are selected as the benchmarks for cases with and without an ODP, respectively.

The simulation setting considers $D = 1\,\mathrm{m}$ and $f_\mathrm{c} = 3\,\mathrm{GHz}$, where the Fresnel distance [53] of the CIS is 20 m.

Fig. 9 shows the root SPEB as a function of the noise level N_0. The figure shows that the introduction of the CIS does not significantly improve the root SPEB in the cases without any ODP. This is because when there is LOS between each anchor and the agent, desirable performance can be achieved even without the help of CIS. However, when an ODP is introduced, with the aid of the CIS, the root SPEB is reduced more than 10 times compared with the scattering plane. This shows that a CIS can mitigate the loss caused by the ODP. The root SPEB is not plotted for the scenario with an ODP but without the scattering plane and the CIS, because the FIM is not full rank in such a case, and the root SPEB is not defined. In this case, the measurements do not provide sufficient information for estimating the position of the agent.

Furthermore, we compare the influence from a focus-on-$\boldsymbol{p}_1$ CIS and a CIS with random phase response distribution. In particular, 1000 random phase responses are obtained, from which the empirical ranges of the root SPEB are determined in the presence of an ODP. The vertical bars in Fig. 9 represent the maximum and minimum of the root SPEB among all

Authorized licensed use limited to: MIT Libraries. Downloaded on June 19,2022 at 19:18:15 UTC from IEEE Xplore. Restrictions apply.

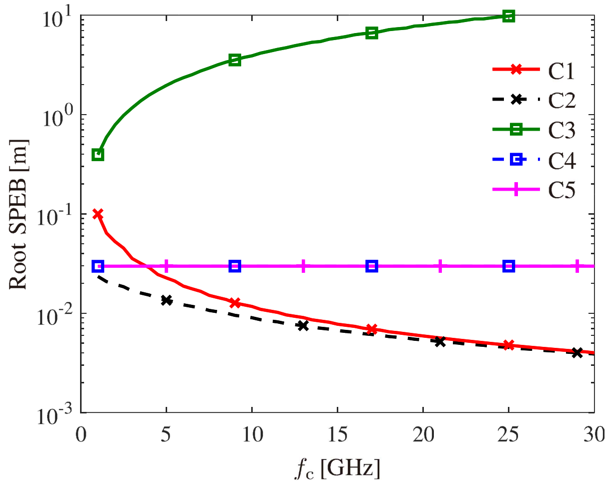

Fig. 10. Impact on the localization accuracy from the carrier frequency of the localization systems.

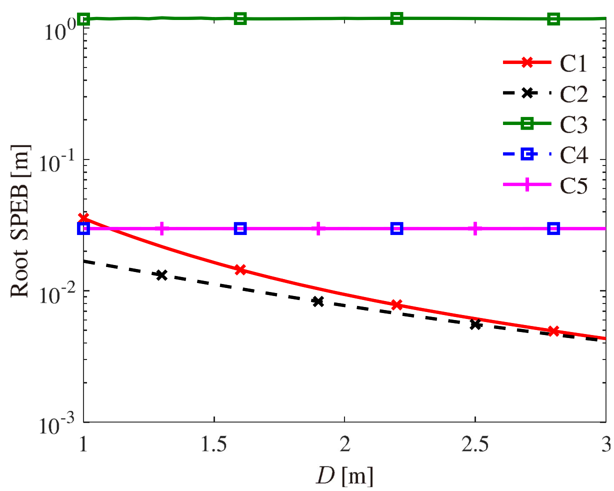

Fig. 11. Impact on the localization accuracy from the size of the CIS or scattering plane.

instantiations of phase response distributions. As shown in Fig. 9, the root SPEB of the localization system with a CIS with the phase response function in (13) is much lower than the lowest root SPEB of the system with a CIS with the uniform phase response distribution, which validates the effectiveness of the phase response function in (13).

In Fig. 10, the carrier frequency of the localization systems varies from 1 GHz to 30 GHz, and the size of the antenna is proportional to λ_0. The Fresnel distance varies correspondingly from 20/3 m to 200 m. Fig. 10 shows that the root SPEB of C5 remains unchanged with the variation of the carrier frequency. This is because the antenna size is considered to be proportional to the wavelength, leading to constant electrical size of the antennas with respect to the carrier frequency f_c. In the situation with an ODP, Fig. 10 shows that the root SPEB of case C1 approaches that of the LOS condition as the frequency increases. From Remark 4, the improvement of the root SPEB of case C1 comes from the relation that $\boldsymbol{J}_k(\boldsymbol{q})$ is approximately proportional to f_c^4. Moreover, the root SPEB of the localization system with a scattering plane does not change significantly with the signal frequency.

In Fig. 11, the size of the CIS or the scattering plane varies from 1 m to 3 m, while the carrier frequency is 3 GHz.

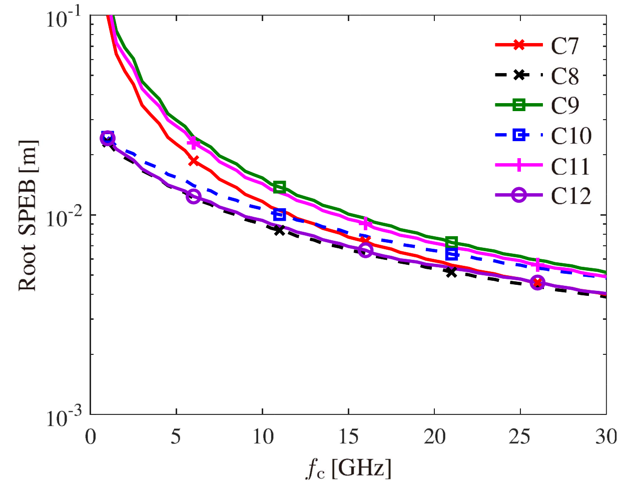

Fig. 12. Impact on the localization accuracy from the carrier frequency of the localization system with the OSP.

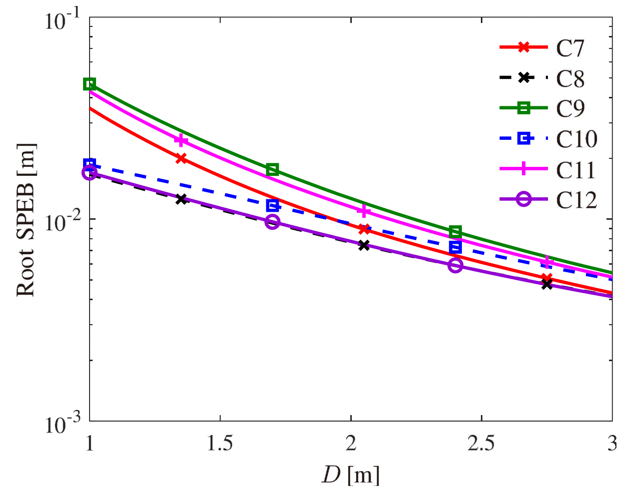

Fig. 13. Impact on the localization accuracy from the size of the CIS with the OSP.

TABLE IV

A NOTATION OF SCENARIO 2

Cases	OSP	ODP	CIS Configuration
C7	0	1	focus-on-$\boldsymbol{p}_1$ CIS
C8	0	0	focus-on-$\boldsymbol{p}_1$ CIS
C9	1	1	focus-on-$\boldsymbol{p}_1$ CIS
C10	1	0	focus-on-$\boldsymbol{p}_1$ CIS
C11	1	1	CIS given by (28) with the priority of $\boldsymbol{p}_1$, $\boldsymbol{p}_2$, $\boldsymbol{p}_3$ from high to low
C12	1	0	CIS given by (28) with the priority of $\boldsymbol{p}_1$, $\boldsymbol{p}_2$, $\boldsymbol{p}_3$ from high to low

Fig. 11 shows a better root SPEB especially in obstructed situation with the size of the CIS. This is because the SNR at the anchors increases as the size of the CIS increases, as shown in Fig. 5. Fig. 11 also shows that the root SPEB of the localization system with the CIS becomes smaller than that in unobstructed situation as the diameter of the OSP increases, which means that the position information from the scattering path via CIS may exceed the position information brought by the direct path. In addition, the root SPEB of case C3 keeps around 1 m for any value of D, and it is significantly higher than other cases.

Authorized licensed use limited to: MIT Libraries. Downloaded on June 19,2022 at 19:18:15 UTC from IEEE Xplore. Restrictions apply.

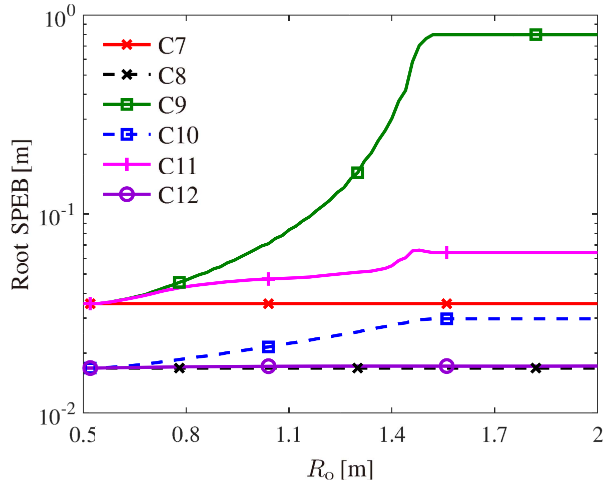

Fig. 14. Impact on the localization accuracy from the size of the OSP.

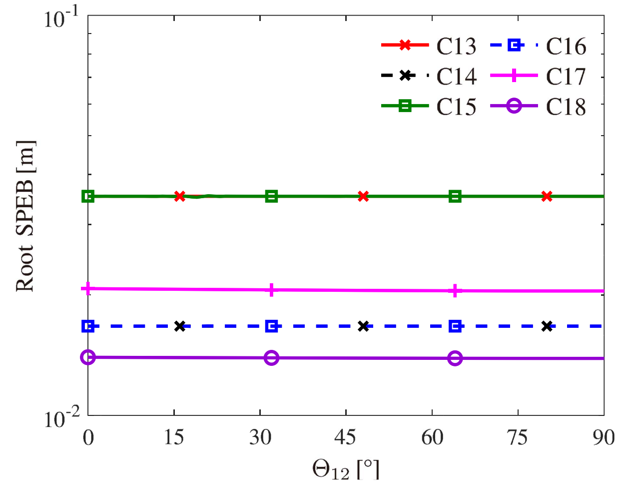

Fig. 15. Impact on the localization accuracy from the relative position of the two CISs or a CIS and a scattering plane.

In Scenario 1, compared with cases without the aid of the CIS, the root SPEB of the CIS-aided cases is reduced significantly as the carrier frequency or the size of the CIS increases. Specially, the root SPEB is reduced about one order of magnitude even if the direct path is obstructed, as shown in Fig. 10 and Fig. 11.

C. Localization With Obstacles on the Scattering Paths

To clarify how the size of the OSP and the size of the CIS affect the transmission of the position information, we consider a spherical OSP whose center is $\boldsymbol{p}_\text{o}$ and radius is R_o. Therefore, for the k-th anchor, its invalid zone on the CIS is given by

$$\mathcal{B}_k = \mathcal{S}_\text{eff} \cap \mathcal{E}_k \tag{32}$$

where $\mathcal{E}_k$ is the elliptical shadow when the k-th anchor illuminates the plane of the CIS.

Fig. 12 and Fig. 13 present the performance of a CIS-aided localization system with OSPs, where the same system parameters of Fig. 10 and Fig. 11 in Section V-A are considered. In addition, we consider a spherical OSP whose center $\boldsymbol{p}_\text{o} = [2, 2, 30]^\text{T}$ (m) and radius $R_\text{o} = 0.8$ m. The cases for Scenario 2 are listed in Table IV.

Fig. 12 shows that as the carrier frequency increases, the root SPEBs of cases C7-C12 approach each other, which means that the deterioration caused by the OSP is weakened. This is due to high carrier frequency enhances the performance of the CIS. Fig. 12 also shows that for the cases whose direct path of the anchor focused by the CIS in the highest priority (C7, C9, C11) are obstructed, the deterioration caused by the OSP is weakened as the frequency increases. This is because the ability of the CIS to enhance position information increases with the carrier frequency, and the invalid zones on the CIS do not change, thus more position information is obtained by the anchors via the scattering paths. By contrast, Fig. 12 shows that for the cases whose direct paths are LOS (C8, C10, C12), the deterioration caused by the OSP is enlarged as the frequency increases. This is because with all LOS paths, the enhancement from the CIS becomes insignificant, and the deterioration due to the invalid zone of CIS is enlarged.

Fig. 13 shows that as the size of the CIS increases, the root SPEBs of cases C7-C12 approach each other, which means that the deterioration caused by OSP is weakened. This is because a larger CIS leads to a smaller ratio of invalid zones for the unchanged OSP.

TABLE V
A NOTATION OF SCENARIO 3

Cases	ODP	Plane Type
C13	1	1 focus-on-$\boldsymbol{p}_1$ CIS with (13)
C14	0	1 focus-on-$\boldsymbol{p}_1$ CIS with (13)
C15	1	Scattering plane + 1 focus-on-$\boldsymbol{p}_1$ CIS with (13)
C16	0	Scattering plane + 1 focus-on-$\boldsymbol{p}_1$ CIS with (13)
C17	1	2 focus-on-$\boldsymbol{p}_1$ CIS with (13)
C18	0	2 focus-on-$\boldsymbol{p}_1$ CIS with (13)

Fig. 14 show that a CIS with the phase response of (28) can perform better than a CIS with the phase response of (13) when there are OSPs. The curves of case C9 and C11 in Fig. 14 shows that if the size of the OSP is relatively large, the CIS configured by (28) with the certain priority performs much better than the focus-on-$\boldsymbol{p}_1$ CIS. This is because CISs configured by (28) with certain priority can combat the deterioration created by the OSP and lack of the LOS path.

D. Localization With Additional CISs

Consider two set-ups: a localization system with two CISs (see Fig. 3), and a localization system with one CIS and one scattering plane whose size $D = 1$ m. The carrier frequency is set as 3 GHz. To study localization with multiple CISs, we evaluate 6 different cases of Scenario 3 as listed in Table V.

Fig. 15 shows that the performance bounds of the localization system with two CISs do not vary significantly as the angle between the two CISs changes, which means that CISs can be deployed flexibly in complex wireless environments, such as a corner of the room. Fig. 15 also shows that the introduction of an additional CIS can improve the root SPEB from 0.035 m to around 0.02 m when one of the direct paths is obstructed, which means that different CISs can cooperate and improve the localization system further. In addition, Fig. 15 also demonstrates that the influence of a scattering plane is insignificant. In particular, the scattering plane hardly affects the root SPEBs, and the slight affection from the scattering plane reduces further as the angle between the CISs decreases.

Authorized licensed use limited to: MIT Libraries. Downloaded on June 19,2022 at 19:18:15 UTC from IEEE Xplore. Restrictions apply.

Fig. 15 shows that the performance gain due to an additional CIS is less significant in Scenario 3 compared to that in Scenario 1. However, the additional CIS still provides about 40% improvement on the root SPEB.

VI. Conclusion

This paper introduced the concept of CISs and established a theoretical framework for location awareness in beyond 5G networks via RISs. Specifically, we presented a general signal model, both for near and far field, for RIS-aided localization and communication based on EM theory. Using this model, we derived the SNR of the received signal and the spectral efficiency of the RIS-aided communications. Then, we established Fisher information analysis for RIS-aided localization. It is shown that the position information intensity of RIS-aided localization is approximately proportional to the fourth power of the carrier frequency, in contrast to the absence of RIS for which it would be a quadratic power. Therefore, the localization performance gain provided by RISs increases significantly with the carrier frequency. We also derived the FIM in the presence of obstacles and multiple RISs. Results show the localization performance gain provided by an RIS with controlled phase response compared to an RIS with random phase responses or a scattering plane. Also, the performance gain provided by a CIS is significantly higher than that provided by a DIS. Furthermore, RISs can improve the robustness of localization systems in the presence of obstructions between transmitting nodes and receiving nodes. The findings in this paper provided guidelines for the design and implementation of RIS-aided NLN for location awareness in beyond 5G networks.

Appendix A

For brevity, the term $\exp\{\jmath 2\pi f_{\mathrm{c}} t\}$ is omitted in the following expressions of fields and potentials, and all these fields and potentials represent sinusoidal waves. The magnetic potential of $\boldsymbol{r}$ generated by the surface current $\boldsymbol{j}(\breve{\boldsymbol{p}})$ on the plane $\mathcal{S}$ is

$$\boldsymbol{a}(\boldsymbol{r}) = \mu \int_{\mathcal{S}} \boldsymbol{j}(\breve{\boldsymbol{p}}) G(\boldsymbol{r}, \boldsymbol{p})\, d\breve{\boldsymbol{p}} \tag{33}$$

with the Green's function $G(\boldsymbol{r}, \boldsymbol{p})$ is given by

$$G(\boldsymbol{r}, \boldsymbol{p}) = \frac{e^{-\jmath\beta|\boldsymbol{r}-\boldsymbol{p}|}}{4\pi|\boldsymbol{r}-\boldsymbol{p}|} \tag{34}$$

where μ denotes the permeability.

Based on Maxwell equations (Lorenz gauge), we have

$$\nabla \times \boldsymbol{e} = -\frac{\partial \boldsymbol{b}}{\partial t} = -\nabla \times \frac{\partial \boldsymbol{a}}{\partial t} \tag{35}$$

$$\boldsymbol{e} = -\nabla\varphi - \frac{\partial \boldsymbol{a}}{\partial t} \tag{36}$$

$$\nabla \cdot \boldsymbol{a} = -\jmath\omega\epsilon\mu\varphi \tag{37}$$

where $\omega = 2\pi f_{\mathrm{c}}$ is the angular frequency, ϵ is permittivity, φ is the electric potential, $\boldsymbol{e}$ is the electric field, and $\boldsymbol{h}$ is the magnetic field.

Therefore, the relation between the magnetic potential $\boldsymbol{a}(\boldsymbol{r})$ and the EM scattering field $\boldsymbol{e}^{\mathrm{s}}$ and $\boldsymbol{h}^{\mathrm{s}}$ is given by

$$\boldsymbol{h}^{\mathrm{s}} = \frac{1}{\mu} \nabla \times \boldsymbol{a} \tag{38}$$

$$\boldsymbol{e}^{\mathrm{s}} = \frac{1}{\jmath\omega\epsilon\mu} \nabla\nabla \cdot \boldsymbol{a} - \jmath\omega\boldsymbol{a}\,. \tag{39}$$

For a perfect electric conductor, the boundary condition at the interface is

$$\boldsymbol{j}(\breve{\boldsymbol{p}}) = \tilde{\boldsymbol{n}} \otimes (\boldsymbol{h}^{\mathrm{i}} + \boldsymbol{h}^{\mathrm{s}}) \tag{40}$$

where $\tilde{\boldsymbol{n}}$ is the surface normal.

According to [54], when the object illuminated by the EM waves is flat, the approximated equivalent current source $\boldsymbol{j}(\breve{\boldsymbol{p}})$ is given by

$$\boldsymbol{j}(\breve{\boldsymbol{p}}) \approx 2\tilde{\boldsymbol{n}} \otimes \boldsymbol{h}^{\mathrm{i}}\,. \tag{41}$$

This approximation assumes that the scattering at each point on the surface takes place as if there is an infinite tangent surface at that point. Note that the approximation holds if the radius of curvature at each point of the surface is large enough [53].

Furthermore, we assume that the phase of the scattered EM waves can be manipulated, and the phase response of the CIS is described as $\Phi_{\mathrm{R}}(\breve{\boldsymbol{p}})$ where $\breve{\boldsymbol{p}} \in \mathcal{S}$ is a point on the interface. Since the scattered waves are generated by the current source, the equivalent current source must take the same phase as the reflected EM waves, given by

$$\boldsymbol{j}_{\Phi}(\boldsymbol{p}) \approx 2\tilde{\boldsymbol{n}} \otimes \boldsymbol{h}^{\mathrm{i}} e^{\jmath\Phi_{\mathrm{R}}(\breve{\boldsymbol{p}})}\,. \tag{42}$$

Substitute (42) into (33), and with (38) and (39), the far-field scattered EM waves are given by

$$\boldsymbol{h}^{\mathrm{s}} = \frac{-\jmath\beta}{2\pi} \int_{\mathcal{S}} \left[\tilde{\boldsymbol{r}} \otimes (\tilde{\boldsymbol{n}} \otimes \boldsymbol{h}^{\mathrm{i}})\right] \frac{e^{-\jmath\beta|\boldsymbol{r}-\boldsymbol{p}|}}{|\boldsymbol{r}-\boldsymbol{p}|} e^{\jmath\Phi_{\mathrm{R}}(\breve{\boldsymbol{p}})}\, d\breve{\boldsymbol{p}} \tag{43}$$

$$\boldsymbol{e}^{\mathrm{s}} = \frac{\jmath\beta\eta}{2\pi} \int_{\mathcal{S}} \left[\tilde{\boldsymbol{r}} \otimes \left[\tilde{\boldsymbol{r}} \otimes (\tilde{\boldsymbol{n}} \otimes \boldsymbol{h}^{\mathrm{i}})\right]\right] \frac{e^{-\jmath\beta|\boldsymbol{r}-\boldsymbol{p}|}}{|\boldsymbol{r}-\boldsymbol{p}|} e^{\jmath\Phi_{\mathrm{R}}(\breve{\boldsymbol{p}})}\, d\breve{\boldsymbol{p}} \tag{44}$$

where η is the wave impedance.

Appendix B

With (A1)-(A2), we derive the scattering field based on Lemma 1 as

$$\boldsymbol{e}_k^{\mathrm{s}} = \frac{\jmath k_0 \eta_0}{2\pi} \int_{\mathcal{S}} \left[\tilde{\boldsymbol{\rho}}_{\mathrm{R},k} \otimes \left[\tilde{\boldsymbol{\rho}}_{\mathrm{R},k} \otimes (\tilde{\boldsymbol{n}} \otimes \boldsymbol{h}_{\mathrm{in}})\right]\right] \times \frac{e^{-\jmath k_0 \rho_{\mathrm{R},k}(\boldsymbol{p})}}{\rho_{\mathrm{R},k}(\boldsymbol{p})} e^{\jmath\Phi_{\mathrm{R}}(\breve{\boldsymbol{p}})}\, d\breve{\boldsymbol{p}} \tag{45}$$

where $\tilde{\boldsymbol{\rho}}_{\mathrm{R},k}$ is the unit vector of $-\boldsymbol{p}_k$, vector $\boldsymbol{h}_{\mathrm{in}}$ is the incident magnetic field intensity on the CIS, $\tilde{\boldsymbol{n}}$ denotes the surface normal, and η_0 is the vacuum wave impedance.

In general, radiation from a finite antenna is a spherical wave, and spherical wave behavior is characterized by $e^{-\jmath k_0 r}/r$ at a distance r away from the antenna [53], i.e.,

$$\boldsymbol{h}_{\mathrm{in}} = H_{\mathrm{T}}(\breve{\boldsymbol{p}}) \frac{e^{-\jmath k_0 \rho_{\mathrm{T}}(\boldsymbol{p})}}{\rho_{\mathrm{T}}(\boldsymbol{p})} s(t)\, \tilde{\boldsymbol{h}}_{\mathrm{in}} \tag{46}$$

where $H_{\mathrm{T}}(\breve{\boldsymbol{p}})$ depends on the antenna size and directivity of the agent, and $s(t)$ is the transmitted baseband signal. Similarly, the incident wave via direct path at the k-th anchor is

$$\boldsymbol{e}_k^{\mathrm{d}} = \eta_0 H_{\mathrm{T}}(\boldsymbol{p}_k) \frac{e^{-\jmath k_0 \rho_{\mathrm{D},k}}}{\rho_{\mathrm{D},k}} s(t)\, \tilde{\boldsymbol{e}}_k^{\mathrm{d}}\,. \tag{47}$$

Authorized licensed use limited to: MIT Libraries. Downloaded on June 19,2022 at 19:18:15 UTC from IEEE Xplore. Restrictions apply.

At the k-th anchor, we have

$$r_k^{\mathrm{s}}(t) = \frac{1}{2\sqrt{2R_{\mathrm{L}}}}\, \boldsymbol{l}_k^{\mathrm{r}}(\mathbf{0}_3)^{\mathrm{H}} \boldsymbol{e}_k^{\mathrm{s}} \tag{48}$$

$$r_k^{\mathrm{d}}(t) = \frac{1}{2\sqrt{2R_{\mathrm{L}}}}\, \boldsymbol{l}_k^{\mathrm{r}}(\boldsymbol{q})^{\mathrm{H}} \boldsymbol{e}_k^{\mathrm{d}} \tag{49}$$

where $\boldsymbol{l}_k^{\mathrm{r}}(\boldsymbol{x})$ is the vector effective length of the antenna at $\boldsymbol{p}_k$ for an EM wave from the position $\boldsymbol{x}$, and $l_k^{\mathrm{r}}(\boldsymbol{x})$ and $\tilde{\boldsymbol{l}}_k^{\mathrm{r}}(\boldsymbol{x})$ denote its modulus and unit vector, respectively.

Furthermore, with the narrow-band assumption, $s(t)$ can be set to 1 and thus can be removed from (46) and (47) for brevity. Substitute (46) into (45) and substitute the result into (48), and substitute (47) into (49), and let $F_k^{\mathrm{s}}(\breve{\boldsymbol{p}}) = \eta_0 H_{\mathrm{T}}(\breve{\boldsymbol{p}}) l_k^{\mathrm{r}}(\mathbf{0}_3)/\sqrt{P_{\mathrm{T}}}, F_k^{\mathrm{d}} = \eta_0 H_{\mathrm{T}}(\boldsymbol{p}_k) l_k^{\mathrm{r}}(\boldsymbol{q})/\sqrt{P_{\mathrm{T}}}, \gamma_k^{\mathrm{s}}(\breve{\boldsymbol{p}}) = \tilde{\boldsymbol{l}}_k^{\mathrm{r}}(\mathbf{0}_3)^{\mathrm{H}}[\tilde{\boldsymbol{\rho}}_{\mathrm{R},k}\otimes[\tilde{\boldsymbol{\rho}}_{\mathrm{R},k}\otimes(\tilde{\boldsymbol{n}}\otimes\tilde{\boldsymbol{h}}_{\mathrm{in}})]]$, and $\gamma_k^{\mathrm{d}} = \tilde{\boldsymbol{l}}_k^{\mathrm{r}}(\boldsymbol{q})^{\mathrm{H}} \tilde{\boldsymbol{e}}_k^{\mathrm{d}}$, we can get (5) and (6) respectively in Proposition 1.

Appendix C

Due to (A3) and (A4), $\max\{\boldsymbol{\sigma}_k^{\mathrm{d}}, \boldsymbol{\sigma}_k^{\mathrm{s}}\} \ll \min\{\boldsymbol{\mu}_k^{\mathrm{d}}, \boldsymbol{\mu}_k^{\mathrm{s}}\}$, and thus $\boldsymbol{\sigma}_k^{\mathrm{d}}$ and $\boldsymbol{\sigma}_k^{\mathrm{s}}$ can be neglected in (17). Define the FIM $\boldsymbol{J}_k^{\mathrm{s}}$, $\boldsymbol{J}_k^{\mathrm{d}}$, and $\boldsymbol{C}_k$ as

$$\boldsymbol{J}_k^{\mathrm{s}}(\boldsymbol{q}) = \frac{P_{\mathrm{T}}}{2P_{\mathrm{n}}R_{\mathrm{L}}}\, \Re\{\boldsymbol{\mu}_k^{\mathrm{s}}(\boldsymbol{\mu}_k^{\mathrm{s}})^{\mathrm{H}}\} \tag{50}$$

$$\boldsymbol{J}_k^{\mathrm{d}}(\boldsymbol{q}) = \frac{P_{\mathrm{T}}}{2P_{\mathrm{n}}R_{\mathrm{L}}}\, \Re\{\boldsymbol{\mu}_k^{\mathrm{d}}(\boldsymbol{\mu}_k^{\mathrm{d}})^{\mathrm{H}}\} \tag{51}$$

$$\boldsymbol{C}_k(\boldsymbol{q}) = \frac{P_{\mathrm{T}}}{2P_{\mathrm{n}}R_{\mathrm{L}}}\, \Re\{\boldsymbol{\mu}_k^{\mathrm{s}}(\boldsymbol{\mu}_k^{\mathrm{d}})^{\mathrm{H}} + \boldsymbol{\mu}_k^{\mathrm{d}}(\boldsymbol{\mu}_k^{\mathrm{s}})^{\mathrm{H}}\}\,. \tag{52}$$

Since the CIS is configured as (13) and the Tx/Rx antennas are small dipole antennas [55] along z-axis whose current maximum is I_0 and length is Δz, (21) and (22) can be expressed respectively as

$$\boldsymbol{\mu}_k^{\mathrm{s}} = -\sqrt{\frac{3\eta_0}{64\pi^3}}\, k_0^2\, \Delta z\, e^{\jmath k_0 \rho_{\mathrm{D},k}} \boldsymbol{u}_k^{\mathrm{s}} \tag{53}$$

$$\boldsymbol{\mu}_k^{\mathrm{d}} = -\sqrt{\frac{3\eta_0}{16\pi}}\, k_0\, \Delta z\, e^{\jmath k_0 \rho_{\mathrm{D},k}} \boldsymbol{u}_k^{\mathrm{d}} \tag{54}$$

where

$$\begin{aligned}\boldsymbol{u}_k^{\mathrm{s}} &= \int_{\mathcal{S}} \frac{\big|[\tilde{\boldsymbol{p}_k}\otimes(\tilde{\boldsymbol{p}_k}\otimes\tilde{\boldsymbol{z}})]^{\mathrm{T}}[\tilde{\boldsymbol{p}_k}\otimes(\tilde{\boldsymbol{p}_k}\otimes(q_3\tilde{\boldsymbol{z}}+(\boldsymbol{p}-\boldsymbol{q})))]\big|}{\big|\tilde{\boldsymbol{p}_k}(\tilde{\boldsymbol{p}_k}^{\mathrm{T}}\tilde{\boldsymbol{z}})-\tilde{\boldsymbol{z}}\big|\big|\tilde{\boldsymbol{z}}\otimes(\boldsymbol{p}-\boldsymbol{q})\big|} \\ &\quad\times \frac{\big|\sin\theta_{\mathrm{T}}(\boldsymbol{p})\big|\big|\sin\theta_k^{\mathrm{r}}\big|}{\rho_{\mathrm{R},k}(\boldsymbol{p})\rho_{\mathrm{T}}(\boldsymbol{p})^2}(\boldsymbol{q}-\boldsymbol{p})\, d\breve{\boldsymbol{p}}\end{aligned} \tag{55}$$

$$\boldsymbol{u}_k^{\mathrm{d}} = \frac{\sin^2\theta_k^{\mathrm{d}}}{\rho_{\mathrm{D},k}^2}(\boldsymbol{q}-\boldsymbol{p}_k) \tag{56}$$

in which $\theta_{\mathrm{T}}(\boldsymbol{p})$ represents the included angle between z-axis and the straight line determined by $\boldsymbol{q}$ and $\boldsymbol{p}$; θ_k^{r} represents the included angle between z-axis and $\boldsymbol{p}_k$; and θ_k^{d} represents the included angle between z-axis and the straight line determined by $\boldsymbol{p}_k$ and $\boldsymbol{q}$.

Furthermore, using the definitions of $\boldsymbol{J}_k^{\mathrm{s}}$, $\boldsymbol{J}_k^{\mathrm{d}}$ and $\boldsymbol{C}_k$, and the fact that $\psi_k^2 = \psi_k$, we obtain (23).

Appendix D

First, consider a system with two CISs, i.e., S1 and S2, as shown in Fig. 3. In this case, the received signal at the k-th anchor is given by

$$\mathsf{r}_k(t) = r_k^{\mathrm{s},1}(t) + r_k^{\mathrm{s},2}(t) + \psi_k r_k^{\mathrm{d}}(t) + \mathsf{n}_k(t) \tag{57}$$

where

$$\begin{aligned}r_k^{\mathrm{s},1}(t) &= \frac{\jmath k_0\sqrt{P_{\mathrm{T}}}}{4\pi\sqrt{2R_{\mathrm{L}}}}\int_{\mathcal{S}_1}\gamma_k^{\mathrm{s}}(\boldsymbol{p})F_k^{\mathrm{s}}(\boldsymbol{p})\frac{e^{-\jmath k_0(\rho_{\mathrm{T}}(\boldsymbol{p})+\rho_{\mathrm{R},k}(\boldsymbol{p}))}}{\rho_{\mathrm{T}}(\boldsymbol{p})\rho_{\mathrm{R},k}(\boldsymbol{p})} \\ &\qquad\times e^{\jmath\Phi_{\mathrm{R}}(\breve{\boldsymbol{p}})}\, d\breve{\boldsymbol{p}}\end{aligned} \tag{58}$$

$$\begin{aligned}r_k^{\mathrm{s},2}(t) &= \frac{\jmath k_0\sqrt{P_{\mathrm{T}}}}{4\pi\sqrt{2R_{\mathrm{L}}}}\int_{\mathcal{S}_2}\gamma_k^{\mathrm{s}}(\boldsymbol{R}(\Theta_{12})\boldsymbol{p}'+\boldsymbol{p}_{\mathrm{S2}}) \\ &\quad\times F_k^{\mathrm{s}}(\boldsymbol{R}(\Theta_{12})\boldsymbol{p}'+\boldsymbol{p}_{\mathrm{S2}})\frac{e^{\jmath k_0\rho_{\mathrm{R},\mathrm{k}}(\boldsymbol{R}(\Theta_{12})\boldsymbol{p}'+\boldsymbol{p}_{\mathrm{S2}})}}{\rho_{\mathrm{R},\mathrm{k}}(\boldsymbol{R}(\Theta_{12})\boldsymbol{p}'+\boldsymbol{p}_{\mathrm{S2}})} \\ &\quad\times\frac{e^{\jmath k_0\rho_{\mathrm{T}}(\boldsymbol{R}(\Theta_{12})\boldsymbol{p}'+\boldsymbol{p}_{\mathrm{S2}})}}{\rho_{\mathrm{T}}(\boldsymbol{R}(\Theta_{12})\boldsymbol{p}'+\boldsymbol{p}_{\mathrm{S2}})}\, e^{-\jmath\Phi_{\mathrm{R},2}(\breve{\boldsymbol{p}}')}\, d\breve{\boldsymbol{p}}'\,.\end{aligned} \tag{59}$$

Following a method similar to that of Proposition 2, we have

$$\begin{aligned}\boldsymbol{J}_k^{\mathrm{M}}(\boldsymbol{q}) = \frac{P_{\mathrm{T}}}{2P_{\mathrm{n}}R_{\mathrm{L}}}\Re\Big\{&\big[\boldsymbol{\mu}_k^{\mathrm{s},1}+\boldsymbol{\sigma}_k^{\mathrm{s},1}+\boldsymbol{\mu}_k^{\mathrm{s},2}+\boldsymbol{\sigma}_k^{\mathrm{s},2} \\ &+\psi_k(\boldsymbol{\mu}_k^{\mathrm{d}}+\boldsymbol{\sigma}_k^{\mathrm{d}})\big]\big[\boldsymbol{\mu}_k^{\mathrm{s},1}+\boldsymbol{\sigma}_k^{\mathrm{s},1} \\ &+\boldsymbol{\mu}_k^{\mathrm{s},2}+\boldsymbol{\sigma}_k^{\mathrm{s},2}+\psi_k(\boldsymbol{\mu}_k^{\mathrm{d}}+\boldsymbol{\sigma}_k^{\mathrm{d}})\big]^{\mathrm{H}}\Big\}\end{aligned} \tag{60}$$

where

$$\begin{aligned}\boldsymbol{\mu}_k^{\mathrm{s},1} &= \frac{\jmath k_0}{2\pi}\int_{\mathcal{S}_1}\gamma_k^{\mathrm{s}}(\boldsymbol{p})F_k^{\mathrm{s}}(\boldsymbol{p})\frac{e^{\jmath k_0\rho_{\mathrm{R},k}(\boldsymbol{p})}}{\rho_{\mathrm{R},k}(\boldsymbol{p})}\frac{e^{\jmath k_0\rho_{\mathrm{T}}(\boldsymbol{p})}}{\rho_{\mathrm{T}}(\boldsymbol{p})^2} \\ &\quad\times\Big(-\jmath k_0+\frac{1}{\rho_{\mathrm{T}}(\boldsymbol{p})}\Big)e^{-\jmath\Phi_{\mathrm{R},1}(\breve{\boldsymbol{p}})}(\boldsymbol{q}-\boldsymbol{p})\, d\breve{\boldsymbol{p}}'\end{aligned} \tag{61a}$$

$$\begin{aligned}\boldsymbol{\sigma}_k^{\mathrm{s},1} &= \frac{-\jmath k_0}{2\pi}\int_{\mathcal{S}_1}\frac{e^{\jmath k_0\rho_{\mathrm{T}}(\boldsymbol{p})}}{\rho_{\mathrm{T}}(\boldsymbol{p})}\,\frac{e^{\jmath k_0\rho_{\mathrm{R},k}(\boldsymbol{p})}}{\rho_{\mathrm{R},k}(\boldsymbol{p})}e^{-\jmath\Phi_{\mathrm{R},1}(\breve{\boldsymbol{p}})} \\ &\quad\times\frac{\partial}{\partial\boldsymbol{q}}\big(\gamma_k^{\mathrm{s}}(\breve{\boldsymbol{p}})F_k^{\mathrm{s}}(\breve{\boldsymbol{p}})\big)d\breve{\boldsymbol{p}}\end{aligned} \tag{61b}$$

$$\begin{aligned}\boldsymbol{\mu}_k^{\mathrm{s},2} &= \frac{\jmath k_0}{2\pi}\int_{\mathcal{S}_2}\gamma_k^{\mathrm{s}}(\boldsymbol{R}(\Theta_{12})\boldsymbol{p}'+\boldsymbol{p}_{\mathrm{S2}})F_k^{\mathrm{s}}(\boldsymbol{R}(\Theta_{12})\boldsymbol{p}'+\boldsymbol{p}_{\mathrm{S2}}) \\ &\quad\times\frac{e^{\jmath k_0\rho_{\mathrm{R},\mathrm{k}}(\boldsymbol{R}(\Theta_{12})\boldsymbol{p}'+\boldsymbol{p}_{\mathrm{S2}})}}{\rho_{\mathrm{R},\mathrm{k}}(\boldsymbol{R}(\Theta_{12})\boldsymbol{p}'+\boldsymbol{p}_{\mathrm{S2}})}\frac{e^{\jmath k_0\rho_{\mathrm{T}}(\boldsymbol{R}(\Theta_{12})\boldsymbol{p}'+\boldsymbol{p}_{\mathrm{S2}})}}{\rho_{\mathrm{T}}(\boldsymbol{R}(\Theta_{12})\boldsymbol{p}'+\boldsymbol{p}_{\mathrm{S2}})^2} \\ &\quad\times\Big(-\jmath k_0+\frac{1}{\rho_{\mathrm{T}}(\boldsymbol{R}(\Theta_{12})\boldsymbol{p}'+\boldsymbol{p}_{\mathrm{S2}})}\Big)e^{-\jmath\Phi_{\mathrm{R},2}(\breve{\boldsymbol{p}}')} \\ &\quad\times\big(\boldsymbol{q}-(\boldsymbol{R}(\Theta_{12})\boldsymbol{p}'+\boldsymbol{p}_{\mathrm{S2}})\big)\, d\breve{\boldsymbol{p}}'\end{aligned} \tag{61c}$$

$$\begin{aligned}\boldsymbol{\sigma}_k^{\mathrm{s},2} &= \frac{-\jmath k_0}{2\pi}\int_{\mathcal{S}_2}\frac{e^{\jmath k_0\rho_{\mathrm{T}}(\boldsymbol{R}(\Theta_{12})\boldsymbol{p}'+\boldsymbol{p}_{\mathrm{S2}})}}{\rho_{\mathrm{T}}(\boldsymbol{R}(\Theta_{12})\boldsymbol{p}'+\boldsymbol{p}_{\mathrm{S2}})} \\ &\quad\times\frac{e^{\jmath k_0\rho_{\mathrm{R},k}(\boldsymbol{R}(\Theta_{12})\boldsymbol{p}'+\boldsymbol{p}_{\mathrm{S2}})}}{\rho_{\mathrm{R},\mathrm{k}}(\boldsymbol{R}(\Theta_{12})\boldsymbol{p}'+\boldsymbol{p}_{\mathrm{S2}})} \\ &\quad\times\frac{\partial}{\partial\boldsymbol{q}}\big(\gamma_k^{\mathrm{s}}(\boldsymbol{R}(\Theta_{12})\boldsymbol{p}'+\boldsymbol{p}_{\mathrm{S2}})F_k^{\mathrm{s}}(\boldsymbol{R}(\Theta_{12})\boldsymbol{p}'+\boldsymbol{p}_{\mathrm{S2}})\big) \\ &\quad\times e^{-\jmath\Phi_{\mathrm{R},2}(\breve{\boldsymbol{p}}')}\, d\breve{\boldsymbol{p}}'\,.\end{aligned} \tag{61d}$$

Here, $\breve{\boldsymbol{p}}' \in \mathcal{S}_2$ is a two-dimensional vector corresponding to $[(\breve{\boldsymbol{p}}')^{\mathrm{T}}, 0]^{\mathrm{T}}$ described in the coordinate system (x', y', z') whose X'-Y' plane is parallel to the CIS S2. Vector $\boldsymbol{p}_{\mathrm{S2}}$ is the origin point of the coordinate system (x', y', z') described in the coordinate system (x, y, z), the rotation matrix

$$\boldsymbol{R}(\Theta_{12}) = \begin{bmatrix}\cos\Theta_{12} & 0 & \sin\Theta_{12} \\ 0 & 1 & 0 \\ -\sin\Theta_{12} & 0 & \cos\Theta_{12}\end{bmatrix}$$

and Θ_{12} is the angle between the CISs S1 and S2, as shown in Fig. 3.

Authorized licensed use limited to: MIT Libraries. Downloaded on June 19,2022 at 19:18:15 UTC from IEEE Xplore. Restrictions apply.

Results for the scenario with two CISs can be extended to scenarios with multiple CISs. In particular, we suppose there are M CISs in the system. For the m-th CIS Sm with $m \in \{1, 2, \dots M\}$, we establish a coordinate system CS_m whose origin point is contained in $\mathcal{S}_m$ and X-Y plane coincides with $\mathcal{S}_m$. Let $\boldsymbol{p}_{\mathrm{S}m}$ be the coordinate of the origin point of CS_m in a basic coordinate system CS_0. We use the rotation matrix $\boldsymbol{R}_m$ to describe the rotation of CS_m compared to CS_0. Then, Corollary 2 can be proved in a similar manner.

Acknowledgment

The authors would like to thank R. Cohen, C. A. Gómez-Vega, G. Kwon, and H. Zhao for their helpful suggestions and careful reading of the manuscript.

References

[1] M. Z. Win *et al.*, "Network localization and navigation via cooperation," *IEEE Commun. Mag.*, vol. 49, no. 5, pp. 56–62, May 2011.

[2] N. Patwari, J. N. Ash, S. Kyperountas, A. O. Hero, R. L. Moses, and N. S. Correal, "Locating the nodes: Cooperative localization in wireless sensor networks," *IEEE Signal Process. Mag.*, vol. 22, no. 4, pp. 54–69, Jul. 2005.

[3] S. Gezici *et al.*, "Localization via ultra-wideband radios: A look at positioning aspects for future sensor networks," *IEEE Signal Process. Mag.*, vol. 22, no. 4, pp. 70–84, Jul. 2005.

[4] A. T. Ihler, J. W. Fisher, R. L. Moses, and A. S. Willsky, "Nonparametric belief propagation for self-localization of sensor networks," *IEEE J. Sel. Areas Commun.*, vol. 23, no. 4, pp. 809–819, Apr. 2005.

[5] E. Paolini, A. Giorgetti, M. Chiani, R. Minutolo, and M. Montanari, "Localization capability of cooperative anti-intruder radar systems," *EURASIP J. Adv. Signal Process.*, vol. 2008, Apr. 2008, Art. no. 726854.

[6] A. A. Saucan and M. Z. Win, "Information-seeking sensor selection for ocean-of-things," *IEEE Internet Things J.*, vol. 7, no. 10, pp. 10072–10088, Oct. 2020.

[7] Y. Yuan, W. Yi, R. Hoseinnezhad, and P. K. Varshney, "Robust power allocation for resource-aware multi-target tracking with colocated MIMO radars," *IEEE Trans. Signal Process.*, vol. 69, pp. 443–458, 2021.

[8] M. Chiani, A. Giorgetti, and E. Paolini, "Sensor radar for object tracking," *Proc. IEEE*, vol. 106, no. 6, pp. 1022–1041, Jun. 2018.

[9] S. Bartoletti, A. Conti, and M. Z. Win, "Device-free counting via wideband signals," *IEEE J. Sel. Areas Commun.*, vol. 35, no. 5, pp. 1163–1174, May 2017.

[10] P. Sharma, A.-A. Saucan, D. J. Bucci, and P. K. Varshney, "Decentralized Gaussian filters for cooperative self-localization and multi-target tracking," *IEEE Trans. Signal Process.*, vol. 67, no. 22, pp. 5896–5911, Nov. 2019.

[11] G. Cardone *et al.*, "Fostering participaction in smart cities: A geo-social crowdsensing platform," *IEEE Commun. Mag.*, vol. 51, no. 6, pp. 112–119, Jun. 2013.

[12] A. Zanella, N. Bui, A. Castellani, L. Vangelista, and M. Zorzi, "Internet of Things for smart cities," *IEEE Internet Things J.*, vol. 1, no. 1, pp. 22–32, Feb. 2014.

[13] G. Pasolini *et al.*, "Smart city pilot projects using LoRa and IEEE802.15.4 technologies," *Sensors*, vol. 18, no. 4, p. 1118, Apr. 2018.

[14] V. Moreno, M. A. Zamora, and A. F. Skarmeta, "A low-cost indoor localization system for energy sustainability in smart buildings," *IEEE Sensors J.*, vol. 16, no. 9, pp. 3246–3262, May 2016.

[15] N. C. Luong, D. T. Hoang, P. Wang, D. Niyato, and D. I. Kim, "Data collection and wireless communication in Internet of Things (IoT) using economic analysis and pricing models: A survey," *IEEE Commun. Surveys Tuts.*, vol. 18, no. 4, pp. 2546–2590, 4th Quart., 2016.

[16] L. Chen *et al.*, "Robustness, security and privacy in location-based services for future IoT: A survey," *IEEE Access*, vol. 5, pp. 8956–8977, 2017.

[17] M. Z. Win, F. Meyer, Z. Liu, W. Dai, S. Bartoletti, and A. Conti, "Efficient multisensor localization for the Internet of Things: Exploring a new class of scalable localization algorithms," *IEEE Signal Process. Mag.*, vol. 35, no. 5, pp. 153–167, Sep. 2018.

[18] D. Miorandi, S. Sicari, F. De Pellegrini, and I. Chlamtac, "Internet of Things: Vision, applications and research challenges," *Ad Hoc Netw.*, vol. 10, no. 7, pp. 1497–1516, Sep. 2012.

[19] S. G. Nagarajan, P. Zhang, and I. Nevat, "Geo-spatial location estimation for Internet of Things (IoT) networks with one-way time-of-arrival via stochastic censoring," *IEEE Internet Things J.*, vol. 4, no. 1, pp. 205–214, Feb. 2017.

[20] *Service Requirements for 5G System*, 3rd Generation Partnership Project 3GPP, document TS 22.261 V18.1.1 (2021-01), Jun. 2021.

[21] B. W. Parkinson, J. J. Spilker, Jr., P. Axelrad, and P. Enge, *Global Positioning System: Theory and Applications* (Progress in Astronautics and Aeronautics), vol. 1. Washington, DC, USA: AIAA Press, 1996.

[22] B. W. Parkinson, J. J. Spilker, Jr., P. Axelrad, and P. Enge, *Global Positioning System: Theory and Applications*, (Progress in Astronautics and Aeronautics), vol. 2. Washington, DC, USA: AIAA Press, 1996.

[23] B. Hofmann-Wellenhof, H. Lichtenegger, and J. Collins, *Global Positioning System: Theory and Practice*, 5th ed. New York, NY, USA: Springer-Verlag Wien, 2001.

[24] Y. Shen and M. Z. Win, "Fundamental limits of wideband localization—Part I: A general framework," *IEEE Trans. Inf. Theory*, vol. 56, no. 10, pp. 4956–4980, Oct. 2010.

[25] Y. Shen, H. Wymeersch, and M. Z. Win, "Fundamental limits of wideband localization—Part II: Cooperative networks," *IEEE Trans. Inf. Theory*, vol. 56, no. 10, pp. 4981–5000, Oct. 2010.

[26] Z. Wang, S. Zheng, Y. Ye, and S. Boyd, "Further relaxations of the semidefinite programming approach to sensor network localization," *SIAM J. Optim.*, vol. 19, no. 2, pp. 655–673, Jul. 2008.

[27] Y. Shen, W. Dai, and M. Z. Win, "Power optimization for network localization," *IEEE/ACM Trans. Netw.*, vol. 22, no. 4, pp. 1337–1350, Aug. 2014.

[28] A. Conti, M. Guerra, D. Dardari, N. Decarli, and M. Z. Win, "Network experimentation for cooperative localization," *IEEE J. Sel. Areas Commun.*, vol. 30, no. 2, pp. 467–475, Feb. 2012.

[29] I. Dokmanic, R. Parhizkar, J. Ranieri, and M. Vetterli, "Euclidean distance matrices: Essential theory, algorithms, and applications," *IEEE Signal Process. Mag.*, vol. 32, no. 6, pp. 12–30, Nov. 2015.

[30] G. Mao, B. Fidan, and B. D. O. Anderson, "Wireless sensor network localization techniques," *Comput. Netw.*, vol. 51, no. 10, pp. 2529–2553, 2007.

[31] B. Teague, Z. Liu, F. Meyer, A. Conti, and M. Z. Win, "Network localization and navigation with scalable inference and efficient operation," *IEEE Trans. Mobile Comput.*, early access, Nov. 3, 2020, doi: 10.1109/TMC.2020.3035511.

[32] Z. Liu, W. Dai, and M. Z. Win, "Mercury: An infrastructure-free system for network localization and navigation," *IEEE Trans. Mobile Comput.*, vol. 17, no. 5, pp. 1119–1133, May 2018.

[33] P. Addesso, S. Marano, and V. Matta, "Estimation of target location via likelihood approximation in sensor networks," *IEEE Trans. Signal Process.*, vol. 58, no. 3, pp. 1358–1368, Mar. 2010.

[34] P. Braca, S. Marano, V. Matta, and P. Willett, "Asymptotic efficiency of the PHD in multitarget/multisensor estimation," *IEEE J. Sel. Topics Signal Process.*, vol. 7, no. 3, pp. 553–564, Jun. 2013.

[35] R. M. Buehrer, H. Wymeersch, and R. M. Vaghefi, "Collaborative sensor network localization: Algorithms and practical issues," *Proc. IEEE*, vol. 106, no. 6, pp. 1089–1114, Jun. 2018.

[36] S. Aditya, A. F. Molisch, and H. M. Behairy, "A survey on the impact of multipath on wideband time-of-arrival based localization," *Proc. IEEE*, vol. 106, no. 7, pp. 1183–1203, Jul. 2018.

[37] S. Safavi, U. A. Khan, S. Kar, and J. M. F. Moura, "Distributed localization: A linear theory," *Proc. IEEE*, vol. 106, no. 7, pp. 1204–1223, Jul. 2018.

[38] M. Z. Win, Y. Shen, and W. Dai, "A theoretical foundation of network localization and navigation," *Proc. IEEE*, vol. 106, no. 7, pp. 1136–1165, Jul. 2018.

[39] A. Conti, S. Mazuelas, S. Bartoletti, W. C. Lindsey, and M. Z. Win, "Soft information for localization-of-things," *Proc. IEEE*, vol. 107, no. 11, pp. 2240–2264, Nov. 2019.

[40] M. Z. Win, W. Dai, Y. Shen, G. Chrisikos, and H. V. Poor, "Network operation strategies for efficient localization and navigation," *Proc. IEEE*, vol. 106, no. 7, pp. 1224–1254, Jul. 2018.

[41] A. Puglielli *et al.*, "A scalable massive MIMO array architecture based on common modules," in *Proc. IEEE Int. Conf. Commun. Workshop (ICCW)*, London, U.K., Jun. 2015, pp. 1310–1315.

[42] S. Hu, F. Rusek, and O. Edfors, "Beyond massive MIMO: The potential of positioning with large intelligent surfaces," *IEEE Trans. Signal Process.*, vol. 66, no. 7, pp. 1761–1774, Apr. 2018.

Authorized licensed use limited to: MIT Libraries. Downloaded on June 19,2022 at 19:18:15 UTC from IEEE Xplore. Restrictions apply.

[43] S. Hu, F. Rusek, and O. Edfors, "Beyond massive MIMO: The potential of data transmission with large intelligent surfaces," *IEEE Trans. Signal Process.*, vol. 66, no. 10, pp. 2746–2758, May 2018.

[44] N. Shlezinger, O. Dicker, Y. C. Eldar, I. Yoo, M. F. Imani, and D. R. Smith, "Dynamic metasurface antennas for uplink massive MIMO systems," *IEEE Trans. Commun.*, vol. 67, no. 10, pp. 6829–6843, Oct. 2019.

[45] N. Shlezinger, G. C. Alexandropoulos, M. F. Imani, Y. C. Eldar, and D. R. Smith, "Dynamic metasurface antennas for 6G extreme massive MIMO communications," *IEEE Wireless Commun.*, vol. 28, no. 2, pp. 106–113, Apr. 2021.

[46] M. D. Renzo *et al.*, "Smart radio environments empowered by reconfigurable intelligent surfaces: How it works, state of research, and road ahead," *IEEE J. Sel. Areas Commun.*, vol. 38, no. 11, pp. 2450–2525, Nov. 2020.

[47] H. Zhang *et al.*, "MetaRadar: Indoor localization by reconfigurable metamaterials," *IEEE Trans. Mobile Comput.*, early access, Dec. 14, 2020, doi: 10.1109/TMC.2020.3044603.

[48] Y. Han, W. Tang, S. Jin, C. Wen, and X. Ma, "Large intelligent surface-assisted wireless communication exploiting statistical CSI," *IEEE Trans. Veh. Technol.*, vol. 68, no. 8, pp. 8238–8242, Jun. 2019.

[49] Q. Wu and R. Zhang, "Intelligent reflecting surface enhanced wireless network via joint active and passive beamforming," *IEEE Trans. Wireless Commun.*, vol. 18, no. 11, pp. 5394–5409, Nov. 2019.

[50] A. Elzanaty, A. Guerra, F. Guidi, and M. Alouini, "Reconfigurable intelligent surfaces for localization: Position and orientation error bounds," *IEEE Trans. Signal Process.*, vol. 69, pp. 5386–5402, 2021.

[51] G. C. Alexandropoulos, N. Shlezinger, and P. del Hougne, "Reconfigurable intelligent surfaces for rich scattering wireless communications: Recent experiments, challenges, and opportunities," *IEEE Commun. Mag.*, vol. 59, no. 6, pp. 28–34, Jun. 2021.

[52] S. M. Kay, *Fundamentals of Statistical Signal Processing: Estimation Theory*. Upper Saddle River, NJ, USA: Prentice-Hall, 1993.

[53] W. L. Stutzman and G. A. Thiele, *Antenna Theory and Design*. Hoboken, NJ, USA: Wiley, 2012.

[54] M. I. Skolnik, *Radar Handbook*. New York, NY, USA: McGraw-Hill, 2008.

[55] C. A. Balanis, *Antenna Theory: Analysis and Design*. Hoboken, NJ, USA: Wiley, 2015.

Ziyi Wang (Graduate Student Member, IEEE) received the B.E. degree (with highest honor) from the School of Electronic and Information Engineering, Beihang University, Beijing, China, in 2020. He has been with the Wireless Information and Network Sciences Laboratory, Massachusetts Institute of Technology (MIT), Cambridge, MA, USA, since September 2020. His research interests include wireless communication, network localization, and reconfigurable intelligent surfaces. He received national scholarships from 2016 to 2018. He served as a Reviewer for the IEEE Transactions on Communications, the IEEE Transactions on Wireless Communications, the IEEE Wireless Communications Letters, and the IEEE International Conference on Communications.

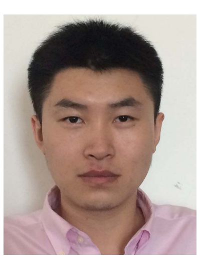

Zhenyu Liu (Graduate Student Member, IEEE) received the B.S. (with honor) and M.S. degrees in electronic engineering from Tsinghua University, Beijing, China, in 2011 and 2014, respectively. He is working toward the Ph.D. degree in networks and statistics with the Massachusetts Institute of Technology (MIT), Cambridge, MA, USA.

Currently, he is a Research Assistant with the Wireless Information and Network Sciences Laboratory, MIT. His research interests include wireless communications, network localization, distributed inference, stochastic optimization, and networked control.

Mr. Liu was the recipient of the first prize of the IEEE Communications Society's Student Competition in 2016 and 2019, the R&D 100 Award for Peregrine System in 2018, and the Best Paper Award at the IEEE Latin-American Conference on Communications in 2017. He is an active member of the IEEE Communications Society's Radio Communications Committee. He served as a reviewer for various IEEE journals and international conferences.

Yuan Shen (Senior Member, IEEE) received the B.E. degree in electronic engineering from Tsinghua University in 2005, and the S.M. and Ph.D. degrees in electrical engineering and computer science from the Massachusetts Institute of Technology (MIT) in 2008 and 2014, respectively.

He is currently a Professor with the Department of Electronic Engineering, Tsinghua University. His current research focuses on network localization and navigation, resource allocation, inference techniques, and cooperative networks.

Dr. Shen's papers have received the IEEE ComSoc Fred W. Ellersick Prize and three best paper awards from IEEE conferences. He has served as the TPC Symposium Co-Chair for IEEE ICC and IEEE GLOBECOM for several times. He was the Elected Chair for the IEEE ComSoc Radio Communications Committee from 2019 to 2020. He is also an Editor of the IEEE Transactions on Communications, IEEE Transactions on Wireless Communications, IEEE Wireless Communications Letters, and *China Communications*.

Andrea Conti (Fellow, IEEE) is a Professor and the Founding Director of the Wireless Communication and Localization Networks Laboratory with the University of Ferrara, Italy. Prior to joining the University of Ferrara, he was with CNIT and with IEIIT-CNR.

In Summer 2001, he was with the Wireless Systems Research Department, AT&T Research Laboratories. Since 2003, he has been a frequent visitor to the Wireless Information and Network Sciences Laboratory with the Massachusetts Institute of Technology, Cambridge, MA, USA, where he presently holds the Research Affiliate appointment. His research interests involve theory and experimentation of wireless communication and localization systems. His current research topics include network localization and navigation, distributed sensing, adaptive diversity communications, and quantum information science.

Dr. Conti has served as an Editor of IEEE journals and chaired international conferences. He was elected Chair of the IEEE Communications Society's Radio Communications Technical Committee and is the Co-Founder of the IEEE Quantum Communications & Information Technology Emerging Technical Subcommittee. He received the HTE Puskás Tivadar Medal, the IEEE Communications Society's Fred W. Ellersick Prize, and the IEEE Communications Society's Stephen O. Rice Prize in the field of Communications Theory. He is an elected Fellow of the IET, and a member of Sigma Xi. He has been selected as an IEEE Distinguished Lecturer.

Moe Z. Win (Fellow, IEEE) is a Professor at the Massachusetts Institute of Technology (MIT) and the Founding Director of the Wireless Information and Network Sciences Laboratory. Prior to joining MIT, he was with AT&T Research Laboratories and with NASA Jet Propulsion Laboratory.

His research encompasses fundamental theories, algorithm design, and network experimentation for a broad range of real-world problems. His current research topics include ultra-wideband systems, network localization and navigation, network interference exploitation, and quantum information science. He has served the IEEE Communications Society as an Elected Member-at-Large on the Board of Governors, as elected Chair of the Radio Communications Committee, and as an IEEE Distinguished Lecturer. Over the last two decades, he held various editorial positions for IEEE journals and organized numerous international conferences. Recently, he has served on the SIAM Diversity Advisory Committee.

Dr. Win is an elected Fellow of the AAAS, the EURASIP, and the IET. He was honored with two IEEE Technical Field Awards: the IEEE Kiyo Tomiyasu Award (2011) and the IEEE Eric E. Sumner Award (2006, jointly with R. A. Scholtz). His publications, coauthored with students and colleagues, have received several awards. Other recognitions include the IEEE Communications Society Edwin H. Armstrong Achievement Award (2016), the Cristoforo Colombo International Prize for Communications (2013), the Copernicus Fellowship (2011) and the *Laurea Honoris Causa* (2008) from the Università degli Studi di Ferrara, and the U.S. Presidential Early Career Award for Scientists and Engineers (2004). He is an ISI Highly Cited Researcher.

Authorized licensed use limited to: MIT Libraries. Downloaded on June 19,2022 at 19:18:15 UTC from IEEE Xplore. Restrictions apply.